

1 **A thin film viscoplastic theory for calving glaciers:**
2 **Towards a bound on the calving rate of glaciers**

J.N. Bassis

3 Department of Climate and Space Science and Engineering, University of
4 Michigan, Ann Arbor, Michigan, USA.

L. Ultee

5 Department of Climate and Space Science and Engineering, University of
6 Michigan, Ann Arbor, Michigan, USA.

Corresponding author: J.N. Bassis, Department of Climate and Space Science and Engineering,
The University of Michigan, Ann Arbor, MI, USA (jbassis@umich.edu)

This is the author manuscript accepted for publication and has undergone full peer review but has not been through the copyediting, typesetting, pagination and proofreading process, which may lead to differences between this version and the [Version of Record](#). Please cite this article as doi: [10.1029/2019JF005160](https://doi.org/10.1029/2019JF005160)

7 **Abstract.** Projections of the growth and demise of ice sheets and glaciers
8 require physical models of the processes governing flow and fracture of ice.
9 The flow of glacier ice has been treated using increasingly sophisticated mod-
10 els. By contrast, fracture, the process ultimately responsible for half of the
11 mass lost from ice sheets through iceberg calving, is often included using *ad*
12 *hoc* parameterizations. In this study we seek to bridge this gap by introduc-
13 ing a model where ice obeys a power-law rheology appropriate for intact ice
14 below a yield strength. Above the yield strength, we introduce a separate
15 rheology appropriate for the flow of heavily fractured ice, where ice defor-
16 mation occurs more readily along faults and fractures. We show that, pro-
17 vided the motion of fractured ice is sufficiently rapid compared to that of
18 intact ice, the behavior of glaciers depends solely on the rheology of intact
19 ice and the yield strength of ice and is insensitive to the precise rheology of
20 fractured ice. Moreover, assuming glacier ice is unyielded allows us to bound
21 the long term average rate of terminus advance, providing a first principles
22 estimate of rates of retreat associated with the marine ice cliff instability. We
23 illustrate model behavior using idealized geometries and climate forcing and
24 show that the model not only exhibits realistic patterns of advance and re-
25 treat, but has the potential to exhibit hysteresis. This hysteresis could pro-
26 vide an explanation for the sudden onset of rapid retreat observed in marine-
27 terminating glaciers.

1. Introduction

28 The Greenland ice sheet is surrounded by glaciers that terminate in near-vertical ice cliffs
29 submerged in the ocean, called tidewater glaciers. Observations show that these marine-
30 based margins in contact with both the atmosphere and ocean are most susceptible to
31 rapid glacier change and radically increased mass loss [e.g., *Benn et al.*, 2007; *Bassis*,
32 2011; *Rignot et al.*, 2011; *Bassis and Walker*, 2012]. Unlike melting, the other dominant
33 contributor to ice sheet and glacier mass loss, iceberg calving—the process where blocks
34 of ice detach from a glacier—can be very rapid and highly episodic [e.g., *Howat et al.*,
35 2005, 2007; *McFadden et al.*, 2011]. Moreover, observations indicate that mass shed from
36 the termini of Greenland’s many tidewater glaciers is responsible for as much as half of
37 annual mass loss from the ice sheet, and that it drives patterns of thinning and acceleration
38 deep inland from the coasts [*Joughin et al.*, 2008; *Rignot et al.*, 2011; *Straneo et al.*, 2013].

39 Rapid disintegration is not limited to Greenland. In the early 1980s, Columbia Glacier,
40 a tidewater glacier in Alaska, transitioned from a decades-long period of stability into
41 a regime of rapid retreat characterized by more than 20 kilometers of terminus retreat
42 and hundreds of meters of thinning [*Meier and Post*, 1987; *Krimmel*, 2001; *O’Neel et al.*,
43 2005; *McNabb et al.*, 2012]. More recently, *DeConto and Pollard* [2016] building on a
44 theoretical model developed by *Bassis and Walker* [2012], have suggested that continued
45 atmospheric warming could trigger a calving instability termed the ‘marine ice cliff in-
46 stability’, destabilizing large portions of West Antarctica with catastrophic consequences
47 for sea level on decadal to century time scales. A similar instability has been invoked
48 to explain Heinrich events—episodic disintegration events from the Laurentide Ice Sheet

49 that sporadically discharged vast armadas of icebergs through the Hudson Strait into the
50 North Atlantic [*Thomas, 1977; Bassis et al., 2017*].

51 Despite iceberg calving's pivotal role in the mass balance and dynamics of glaciers, it
52 remains poorly understood, defying convenient parameterization in the large-scale nu-
53 merical ice sheet/glacier models used for sea level rise projections [*Benn et al., 2007*].
54 Attempts to parameterize the iceberg calving process have traditionally focused on for-
55 mulating models for fractures, assuming that an iceberg will detach when either a surface
56 or bottom crevasse penetrates the entire thickness or some critical fraction thereof [e.g.,
57 *Weertman, 1980; Rist et al., 2002; Benn et al., 2007; Nick et al., 2010; Bassis and Ma,*
58 *2015*]. These models can be tuned to successfully reproduce large-scale patterns of glacier
59 retreat, but complications remain. For example, researchers typically focus on tensile fail-
60 ure, ignoring the potential for shear failure [*Bassis and Walker, 2012; Bassis and Jacobs,*
61 *2013*]. Moreover, these models often use the depth of surface melt water filling surface
62 crevasses as a tuning parameter that can be adjusted to match observations [e.g., *Nick*
63 *et al., 2010*].

64 Alternatively, it is possible to describe fracture using a bulk phenomenological approach,
65 such as continuum damage mechanics [e.g., *Pralong and Funk, 2005; Duddu et al., 2013;*
66 *Albrecht and Levermann, 2012; Duddu et al., 2013; Borstad et al., 2012b*]. Damage me-
67 chanics models introduce a scalar (or occasionally tensor) damage variable that evolves
68 in response to the stress field [e.g., *Duddu et al., 2013; Borstad et al., 2012b; Pralong and*
69 *Funk, 2005*]. Damage-based models are not limited by the instantaneous steady-state as-
70 sumptions intrinsic to most fracture mechanics based approaches and are able to account
71 for the slow, progressive accumulation of damage. However, it remains unclear how to

72 specify damage evolution; current theories either treat damage evolution heuristically or
73 fit curves to limited laboratory experiments [e.g., *Pralong and Funk*, 2005; *Borstad et al.*,
74 2012a; *Duddu et al.*, 2013; *Bassis and Ma*, 2015; *Borstad et al.*, 2016]. More recently, dis-
75 crete element models have been used to simulate the flow and fracture of highly fractured
76 glacier ice [*Bassis and Jacobs*, 2013; *Astrom et al.*, 2014]. Granular models, unfortunately,
77 are too computationally expensive to include in modern continental-scale ice sheet mod-
78 els and are primarily used to examine the shorter time scale processes associated with
79 individual calving events.

80 The granular hypothesis of fractured ice sheet flow inherent in discrete element models
81 is reminiscent of early theories of ice deformation based on plasticity theory, in which
82 the ice was assumed to deform only once the stress exceeded a yield criterion [*Nye*, 1957;
83 *Cuffey and Paterson*, 1994]. In this study, instead of trying to explicitly incorporate
84 the fracture of ice into a continuum model, we follow a suggestion recently proposed by
85 *Bassis and Jacobs* [2013] and *Bassis and Walker* [2012] and attempt to explain patterns
86 of glacier retreat by assuming that heavily fractured ice deforms more readily than intact
87 ice along pre-existing faults and fractures. Consistent with this hypothesis, we formulate a
88 continuum model in which ice flows slowly like a power-law fluid beneath a yield stress, but
89 fails above a critical yield strength, a type of approximation frequently used to simulate
90 geological fractures within the framework of continuum mechanics [e.g., *Dahlen*, 1990;
91 *Moresi et al.*, 2003; *O'Neill et al.*, 2006].

2. Outline of paper

92 The bulk of this study is devoted to formulating and exploring the consequences of a
93 newly proposed rheology for ice that allows ice to deform rapidly above a yield strength.

94 The key hypothesis of this study (illustrated in Figures 3 and 5) is that ice has a yield
95 strength and, above the yield strength, the effective viscosity of fractured ice is much
96 lower than for intact ice. When the effective stress exceeds the yield strength, the frac-
97 tured/yielded ice will deform rapidly exposing the boundary separating yielded and intact
98 ice as the calving front. In this situation, the migration of the boundary separating intact
99 and yielded ice will then describe the migration of the calving front. Readers uninterested
100 in the mathematical exposition provided may want to skip to sections 6 and 7. It is in
101 these sections where we derive a bound on calving rates associated with the marine ice
102 cliff instability and provide more concrete examples of how the bound can be implemented
103 in numerical ice sheet/glacier models. The paper is structured as follows: In section 3 we
104 start by presenting the newly proposed bi-viscous rheology and non-dimensionalization
105 scheme used to make approximations. Next, in section 4, we proceed by making the thin
106 film approximation to derive the equivalent to the usual ‘shallow ice’ and ‘shallow shelf’
107 approximations appropriate for our yield-strength dependent rheology. In section 5, we
108 examine the limiting case when the state of stress within the glacier first approaches the
109 yield strength of ice. In this limiting case, our model reproduces the perfect plastic ap-
110 proximation previously examined by *Ultee and Bassis* [2016]. Moreover, we show that in
111 the perfect plastic approximation, the yield strength of ice provides a boundary condition
112 on the ice thickness at the terminus. In section 6 we build on the results from section
113 5 and show that provided the effective viscosity of yielded ice is small compared to the
114 effective viscosity of intact ice, the effective stress everywhere must always be less than
115 the yield strength of ice. Crucially, this provides a bound on the ice thickness at the
116 terminus identical to the bound provided by *Bassis and Walker* [2012] (section 5.1, Equa-

tion 48). Moreover, we show that the inequality on the ice thickness near the terminus
 can be manipulated to provide a long-term bound on the calving rates of glaciers (section
 6.2, Equation 54). Our bound on the retreat rate, unlike the empirical parameterization
 proposed by *DeConto and Pollard* [2016], depends on the glacier geometry (ice thickness,
 bed slope and gradient in ice thickness) and climate forcing. Finally, in section 7, we
 provide some numerical examples to illustrate model behavior.

3. Model description

3.1. Governing equations

Denoting the fluid velocity and pressure fields by $(u(x, z, t), w(x, z, t))$ and $p(x, z, t)$,
 respectively, conservation of mass and momentum can be expressed in two dimensions as
 follows (Figure 1):

$$\rho(u_t + uu_x + ww_z) = -p_x + \partial_x \tau_{xx} + \partial_z \tau_{xz}, \quad (1a)$$

$$\rho(w_t + uw_x + ww_z) = -p_z + \partial_x \tau_{xz} - \partial_z \tau_{xx} - \rho g, \quad (1b)$$

$$u_x + w_z = 0, \quad (1c)$$

where ρ is the density of ice (910 kg/m³) and g is the acceleration due to gravity (9.8
 m/s²). In the equations above, we denote partial derivatives with italic subscripts except
 when used to denote components of the deviatoric stress tensor (τ_{xx} , τ_{xz}), and we denote
 partial derivatives of deviatoric stress components by ∂_i . Components of the strain rate
 tensor are given by:

$$\dot{\varepsilon}_{ij} = \frac{1}{2} \left(\frac{\partial u_i}{\partial x_j} + \frac{\partial u_j}{\partial x_i} \right), \quad (2)$$

allowing us to define the second invariant of the strain rate:

$$\dot{\gamma} = \sqrt{\dot{\varepsilon}_{xx}^2 + \dot{\varepsilon}_{xz}^2}. \quad (3)$$

3.2. Rheology

132 Traditionally, a power-law creep rheology called Glen’s law is invoked to describe the
 133 flow of ice [e.g., *Cuffey and Paterson, 1994*]. However, both laboratory and field ob-
 134 servations [e.g., *Vaughan, 1993; Schulson, 2001; Schulson and Duval, 2009*] find that ice
 135 undergoes brittle failure when stress exceeds a critical value called the yield strength.
 136 Brittle failure permits motion along newly formed (or pre-existing) faults and fractures
 137 within the ice, resulting in an abrupt increase in deformation rates. To accomodate this
 138 behavior, we consider a constitutive relationship that generalizes Glen’s flow law such that
 139 glacier deformation only follows the usual power-law creep relationship for stresses up to
 140 a yield strength τ_y . When stress exceeds the yield strength, we assume that enhanced
 141 deformation along pre-existing fractures and faults results in a much smaller effective vis-
 142 cosity. We (crudely) approximate this behavior as power-law creep with effective viscosity
 143 much lower than that of intact ice. Using subscripts (i, j) to denote coordinates (x, z) ,
 144 our bi-viscous rheology can be expressed in the form:

$$\tau_{ij} = \begin{cases} B_i \dot{\gamma}^{\frac{1}{n}-1} \dot{\epsilon}_{ij} & \text{for } \tau < \tau_y \\ \frac{1}{\dot{\gamma}} \left(B_f \dot{\gamma}^{1/n} + \left(1 - \frac{B_f}{B_i}\right) \tau_y \right) \dot{\epsilon}_{ij} & \text{for } \tau \geq \tau_y, \end{cases} \quad (4)$$

145 where (B_i, B_f) represent the rheological hardness parameters for intact and yielded ice,
 146 respectively, $\tau = \sqrt{\tau_{xx}^2 + \tau_{xz}^2}$ denotes the effective stress (in two dimensions) and n is the
 147 flow law exponent for ice (typically 3). Effectively, Equation 4 defines an abrupt transition
 148 from an intact ice rheology to a much weaker failed—or yielded—rheology, similar to what
 149 is observed in laboratory experiments [*Schulson, 2001; Schulson and Duval, 2009*]. The
 150 region of transition from unyielded to yielded ice is called a yield surface, and components
 151 of the stress and strain rate tensors (along with their invariants) are continuous across
 152 the yield surface.

153 The advantage of the bi-viscous approach is that it reduces to the power-law rheology
154 conventionally used by ice sheet modelers when the stress is beneath the yield strength, but
155 accounts for rapid deformation of fractured ice above the yield strength. This transition
156 from intact to failed ice is analogous to damage mechanics, except that here, the transition
157 to failed ice occurs instantaneously instead of over a time scale determined by a heuristic
158 damage production function [e.g., *Pralong and Funk*, 2005; *Duddu et al.*, 2013]. In the
159 absence of data to better constrain the rheology of yielded ice, we focus our mathematical
160 exposition on the simple bi-viscous rheology defined by Equation 4 as a limiting case. We
161 treat B_i and B_f as constant parameters, ignoring any temperature dependence.

162 Figure 2 illustrates effective stress and strain rate for three cases of the bi-viscous
163 rheology, distinguished by different values of the ratio B_f/B_i . As B_f/B_i tends toward
164 zero, the effective stress is limited to the yield strength. This special case generalizes the
165 perfect plastic rheology proposed by *Ultee and Bassis* [2016] and *Nye* [1957] such that
166 unyielded ice is allowed the usual power-law creep deformation rather than assumed to
167 be rigid.

3.3. Boundary conditions

168 Denoting the surface and bottom elevation of the glacier by $s(x, t)$, and $b(x)$, respec-
169 tively, we apply the usual kinematic boundary condition $s_t + us_x = w + \dot{a}$ at the surface,
170 where the accumulation rate \dot{a} measures the net rate at which mass is added or removed
171 from the glacier surface (units of meters of ice equivalent per unit time). We also impose
172 the condition that the upper surface of the glacier is traction-free, neglecting the small

173 gradients in atmospheric pressure over the ice sheet:

$$\left. \begin{aligned} (\tau_{xx} - p) s_x &= \tau_{xz} \\ \tau_{zz} - \tau_{xz} s_x &= p \end{aligned} \right\} z = s(x, t). \quad (5)$$

174 At the base of the ice, we impose a no-penetration boundary condition, resulting in the
175 requirement that $ub_x = w$, neglecting the (small) freezing/melting that can occur beneath
176 grounded glaciers. Defining the basal shear traction

$$\tau_{\parallel} = -\frac{2\tau_{xx}b_x + (1 - b_x^2)\tau_{xz}}{1 + b_x^2}, \quad (6)$$

177 we assume basal sliding only occurs when $|\tau_{\parallel}|$ exceeds the yield strength of the bed τ_b .
178 This sliding law allows the bed to transition between frozen (no-slip) and sliding. Thus,
179 at $z = b(x, t)$ we impose

$$\tau_{\parallel} = \tau_b \frac{u_{\parallel}}{|u_{\parallel}|} + \beta^2 |u_{\parallel}|^{m-1} u_{\parallel}, \quad |\tau_{\parallel}| \geq \tau_b, \quad (7)$$

$$u = w = 0, \quad |\tau_{\parallel}| < \tau_b \quad (8)$$

180 where $u_{\parallel} = (u + wb_x)/\sqrt{1 + b_x^2}$ is the component of ice velocity tangent to the bed, β
181 an empirical sliding parameter, and m the sliding law exponent. This sliding law splices
182 together a Weertman-type sliding law with a plastic sliding law [e.g., *Cuffey and Paterson,*
183 1994]. We recover the Weertman-type sliding law in the limit that τ_b vanishes, and the
184 plastic sliding law when β tends to zero.

185 Finally, we assume a near-vertical calving face at $x = L(t)$ where we require continuity
186 of traction at the ice-air and ice-water portions of the interface,

$$\left. \begin{aligned} \tau_{xx} - p &= \rho_w g \langle z \rangle \\ \tau_{xz} &= 0 \end{aligned} \right\} x = L(t). \quad (9)$$

187
188 Here the angle brackets are defined such that $\langle f \rangle = 0$ when $f \geq 0$ and $\langle f \rangle = f$ when
189 $f < 0$. We take $z = 0$ to represent mean sea level.

190 There are three flow regimes of interest. The first flow regime corresponds to the flow
 191 of intact ice where the effective stress is everywhere less than the yield strength of ice.
 192 This regime is appropriate for the flow of glaciers that lack active calving margins. The
 193 second flow regime occurs when the stress invariant exceeds the yield strength so that the
 194 entire glacier is yielded (disarticulated flow of *mélange*). The third flow regime, illustrated
 195 in Figure 3, corresponds to a situation where the stress invariant at the calving front is
 196 perched at the yield strength, permitting both the flow of intact ice in the interior and
 197 active calving along the ice-ocean interface. It is this third flow regime that is most
 198 relevant for calving glaciers and the one we focus on here.

3.4. Non-dimensionalization

199 We define a characteristic ice sheet thickness H_0 and horizontal length L_0 . We scale
 200 the velocity components, u and w , by U_0 and H_0U_0/L_0 , respectively, and scale time by
 201 L_0/U_0 . We then set:

$$\begin{aligned}
 x &= L_0\tilde{x}, & z &= H_0\tilde{z}, & h &= H_0\tilde{h}, & b &= H_0\tilde{b}, & t &= (L_0/U_0)\tilde{t}, & \dot{a} &= (H_0U_0/L_0)\tilde{a} \\
 \tau_{xz} &= \beta^2U_0^m\tilde{\tau}_{xz}, & \tau_{xx} &= B_i(U_0/L_0)^{1/n}\tilde{\tau}_{xx}, & \tau_{zz} &= B_i(U_0/L_0)^{1/n}\tilde{\tau}_{zz}, & p &= \rho gH_0\tilde{p}, \\
 \gamma &= \frac{U_0}{L_0}\tilde{\gamma}, & \tau &= \beta^2U_0^m\tilde{\tau},
 \end{aligned}$$

202 where the tilde indicates dimensionless variables. We also define the dimensionless yield
 203 strength $T_y = \tau_y L_0 / (\rho g H_0^2)$ and dimensionless basal yield strength $T_b = \tau_b L_0 / (\rho g H_0^2)$.

204 To ease the expansion, we set $\beta^2 U_0^m = \rho g H_0^2 / L_0$, anticipating that stresses associated
 205 with sliding are order unity for calving glaciers. With these definitions the model dynamics
 206 depend on three dimensionless numbers,

$$\epsilon = \frac{H_0}{L_0}, \quad \nu = \frac{B_f}{B_i}, \quad \delta = \frac{B_i (U_0/L_0)^{1/n}}{\rho g H_0}. \quad (10)$$

207 The aspect ratio ϵ is small for all cases we consider here. The viscosity ratio ν , also
 208 assumed to be small for our analysis, compares the characteristic hardness of yielded
 209 and unyielded ice. The parameter δ is the ratio of the longitudinal deviatoric stress to
 210 the hydrostatic pressure and will be large or small, depending on the relative magnitude
 211 of basal friction and longitudinal stresses. We also define the dimensionless Reynolds
 212 number, $\text{Re} = U_0^2 L_0^2 / (g H_0^3)$. The Reynolds number may become large during the quasi-
 213 rigid body detachment of icebergs, but over the typically longer time scales associated
 214 with the evolution of glaciers and ice sheets we anticipate that Re will remain order unity
 215 or less.

216 Non-dimensionalizing and dropping the tilde decoration, the incompressibility condition
 217 remains the same, and the conservation of momentum equations become:

$$\epsilon^2 \text{Re} (u_t + uu_x + ww_z) = -p_x + \delta \partial_x \tau_{xx} + \partial_z \tau_{xz}, \quad (11a)$$

$$\epsilon^4 \text{Re} (w_t + ww_x + ww_z) = -p_z + \epsilon^2 \partial_x \tau_{xz} - \delta \partial_z \tau_{xx} - 1, \quad (11b)$$

218 So long as $\epsilon^2 \text{Re}$ remains small, as expected for long time scales, we can neglect the inertial
 219 terms on the left hand side of Equation 11a and 11b.

220 The dimensionless deviatoric stress and strain rate invariants become:

$$\tau = \sqrt{\frac{\delta^2}{\epsilon^2} \tau_{xx}^2 + \tau_{xz}^2}, \quad \dot{\gamma} = \frac{1}{\epsilon} \sqrt{\epsilon^2 u_x^2 + \frac{1}{4} (u_z + \epsilon^2 w_x)^2}. \quad (12)$$

221 Recalling the dimensionless yield strength $T_y = \tau_y L_0 / (\rho g H_0^2)$, the bi-viscous rheology can
 222 be written:

$$\left. \begin{aligned} \tau_{xx} &= \dot{\gamma}^{1/n-1} u_x \\ \tau_{xz} &= \frac{1}{2} \frac{\delta}{\epsilon^2} \dot{\gamma}^{1/n-1} (u_z + \epsilon^2 w_x) \end{aligned} \right\} \tau < T_y, \quad (13)$$

223 and

$$\left. \begin{aligned} \tau_{xx} &= \left[(1 - \nu) \frac{\epsilon}{\delta} \frac{T_y}{\dot{\gamma}} + \nu \dot{\gamma}^{1/n-1} \right] u_x \\ \tau_{xz} &= \frac{1}{2\epsilon} \left[(1 - \nu) \frac{T_y}{\dot{\gamma}} + \nu \frac{\delta}{\epsilon} \dot{\gamma}^{1/n-1} \right] (u_z + \epsilon^2 w_x) \end{aligned} \right\} \tau \geq T_y. \quad (14)$$

224 The surface boundary conditions at $z = s(x, t)$ become:

$$(\delta\tau_{xx} - p) s_x = \tau_{xz}, \quad (15a)$$

$$-\epsilon^2 \tau_{xz} s_x + \delta\tau_{zz} = p. \quad (15b)$$

225 With the aid of the dimensionless basal traction vector:

$$\tau_{\parallel} = \frac{-2\delta\tau_{xx}b_x + (1 - \epsilon^2b_x^2)\tau_{xz}}{1 + \epsilon^2b_x^2}, \quad (16)$$

226 the basal boundary conditions of Equations 7-8 become $u = w = 0$ for $\tau_{\parallel} < T_b$ and

$$\tau_{\parallel} = \left(\frac{T_b}{|u_{\parallel}|} + |u_{\parallel}|^{m-1} \right) u_b, \quad \tau_{\parallel} \geq T_b, \quad (17)$$

227 with $u_{\parallel} = (u + \epsilon^2 w b_x) / \sqrt{1 + \epsilon^2 b_x^2}$.

228 At the calving front, the condition $\tau_{xz} = 0$ remains the same, but the non-dimensional
229 version of the longitudinal stress component of the calving front boundary condition ap-
230 plied at $x = L(t)$ can now be written,

$$\delta\tau_{xx} - p = \frac{\rho_w}{\rho} \langle z \rangle, \quad x = L(t). \quad (18)$$

4. Thin film approximation

4.1. Preliminaries

231 The thin film approximation proceeds by dropping terms of $\mathcal{O}(\epsilon)$ or smaller from Equations
232 10–18. Equations 11a-11b become:

233

$$\delta\partial_x\tau_{xx} + \partial_z\tau_{xz} = p_x, \quad (19a)$$

$$-\delta\partial_z\tau_{xx} = p_z + 1. \quad (19b)$$

234 Integrating Equation 19b over the ice thickness and applying the surface boundary con-
 235 dition, defined by Equation 15b, we find that to $\mathcal{O}(\epsilon^2)$,

$$p = (s - z) - \delta\tau_{xx}. \quad (20)$$

236 We can use Equation 20 to simplify the boundary condition at $x = L(t)$. We still require
 237 $\tau_{xz} = 0$, but substituting Equation 20 into Equation 18 and integrating over the depth, we
 238 obtain a force balance condition that must be satisfied at the calving front [e.g., *Van der*
 239 *Veen*, 1999]:

$$\delta\bar{\tau}_{xx} = \frac{h}{4} \left(1 - \frac{\rho_w d^2}{\rho h^2} \right) = \frac{h}{4} (1 - r^2), \quad x = L(t), \quad (21)$$

240 where $\bar{\tau}_{xx}$ denotes the depth averaged longitudinal deviatoric stress, h is the ice thickness
 241 and d is the depth from the surface of the ocean to the bottom of the glacier (Figure 1)
 242 with $r^2 \equiv \rho_w d^2 / (\rho h^2)$. Equation 21 provides the form of the boundary condition to be
 243 enforced at the calving front in ‘shallow’ models.

244 Standard integration of the continuity equation and application of kinematic boundary
 245 conditions further yields an evolution equation for ice thickness:

$$H_t + Q_x = \dot{a}, \quad (22)$$

246 where the ice flux $Q = \int_b^s u dz$.

247 Just as for traditional ice sheet models, the limits $\delta \ll 1$ and $\delta \sim 1$ correspond to
 248 important limiting cases of the dynamics. As we show next, $\delta \ll 1$ corresponds to the

249 viscoplastic equivalent of the ‘shallow ice approximation’ used to simulate glaciers where
 250 vertical shear stresses dominate the force balance. In contrast, $\delta \sim 1$ corresponds to
 251 the ‘shelfy-stream approximation’, applied to rapidly sliding glaciers where longitudinal
 252 stresses play an important role in the force balance.

4.2. Small horizontal extensional stresses

253 The first case we consider treats both ϵ and δ as small parameters ($\delta \ll 1$, $\epsilon \ll 1$). Small
 254 δ corresponds to a situation where the pressure gradient is primarily balanced by gradients
 255 in the vertical shear stress, implying that resistance from basal drag plays a dominant role
 256 in resisting flow. This includes the case of a glacier frozen to its bed. Here we shall find
 257 that, provided the viscosity ratio ν is small, the yield strength of ice limits the maximum
 258 ice surface slope, as in the perfect plastic approximation.

259 When $\delta \ll 1$ and $\epsilon \ll 1$, we find from Equation 20 that pressure is hydrostatic. An-
 260 ticipating that vertical shear dominates the flow regime, we pose an expansion of the
 261 form:

$$u = u_0(x, z, t) + \epsilon u_1(x, z, t) + \dots, \quad (23)$$

262 where the indices correspond to the order of ϵ in each term of the expansion. Dropping
 263 terms of order δ we find from Equation 12 that $\dot{\gamma}_0 = (2\epsilon)^{-1} |\partial_z u_0|$, $\tau = |\tau_{xz}|$ and, upon
 264 using the traction-free surface boundary condition given by Equation 15b, we can integrate
 265 Equation 19a to find:

$$\tau_{0xz} = -s_x(s - z). \quad (24)$$

266 The maximum shear stress occurs at the bed and decreases towards the surface. Recall-
 267 ing Equations 12 and 24, it is now apparent that to leading order the effective stress is
 268 $\tau = |s_x|(s - z)$. When $h|s_x| < T_y$, yielding does not occur and deformation occurs solely

269 through slow creeping flow of intact ice. This, however, is precisely the shallow ice ap-
 270 proximation (SIA) frequently used in ice sheet modeling [e.g, *Greve and Blatter, 2009*],
 271 albeit with a basal-yield-strength-dependent sliding law.

272 The horizontal velocity can be decomposed into a component due to sliding \mathcal{U} and a
 273 component due to internal deformation of the ice \mathcal{D} such that the total velocity u is given
 274 by $u_0 = \mathcal{U}_0 + \mathcal{D}_0$. Recalling Equation 17, we can express the sliding velocity \mathcal{U} in terms
 275 of the shear stress:

$$\begin{aligned} \mathcal{U}_0 &= 0, & |s_x| h < T_b \\ \mathcal{U}_0 &= - (h |s_x| - T_b)^{1/m} \frac{s_x}{|s_x|}, & |s_x| h \geq T_b. \end{aligned} \quad (25)$$

276 Investigating the deformational component of the velocity, we follow *Balmforth and Cras-*
 277 *ter* [1999] and define a yield surface, $Y(x, t)$, demarking the boundary between intact ice
 278 (above) and yielded ice (below):

$$z = Y = \max \left(s - \frac{T_y}{|s_x|}, b(x) \right), \quad (26)$$

279 whence beneath the yield strength, deviatoric stresses take the leading order form:

$$\tau_{0xz} = \frac{\delta}{\epsilon^{\frac{1}{n}+1} 2^{1/n}} |\partial_z u_0|^{\frac{1}{n}-1} \partial_z u_0. \quad (27)$$

280 Above the yield strength, the stresses are slightly more complex with leading order form

$$\tau_{0xz} = \left[(1 - \nu) \frac{T_y}{|\partial_z u_0|} + \nu \frac{\delta}{\epsilon^{\frac{1}{n}+1}} \frac{|\partial_z u_0|^{\frac{1}{n}-1}}{2^{1/n}} \right] \partial_z u_0. \quad (28)$$

281 Here we have adopted the more cumbersome (∂_x, ∂_z) notation for partial derivatives to
 282 avoid confusing subscripts labeling the order of terms in the expansion with those indi-
 283 cating partial derivatives.

284 We can substitute Equations 27–28 into Equation 24 to find the deformational compo-
 285 nent of the glacier velocity. After performing the vertical integration, we find

$$\mathcal{D}_0 = -2 \frac{\epsilon^{n+1} |s_x|^{n-1} s_x}{\nu^n \delta^n} \frac{s_x}{n+1} \left\{ [Y - b + \nu(s - Y)]^{n+1} - [Y - z + \nu(s - Y)]^{n+1} \right\}, \quad (29)$$

286 in the yielded region $z \leq Y$ and

$$\mathcal{D}_0 = -2 \frac{\epsilon^{n+1} |s_x|^{n-1} s_x}{\nu^n \delta^n} \frac{s_x}{n+1} \left\{ \nu^n [(s - Y)^{n+1} - (s - z)^{n+1}] + \right. \\ \left. [(Y - b) + \nu(s - Y)]^{n+1} - \nu^{n+1} (s - Y)^{n+1} \right\}, \quad (30)$$

287 in the intact region $z > Y$. The deformational velocity of intact ice is small unless
 288 $\delta \leq \epsilon^{1+\frac{1}{n}}$, whereas for failed ice, deformational velocity is small unless $\nu\delta \leq \epsilon^{1+\frac{1}{n}}$.

289 The characteristics of the vertical velocity profile are illustrated in Figure 4 for various
 290 values of ν . Taking the limit $\nu \rightarrow 0$, i.e. $B_f \ll B_i$, we recover the Herschel-Bulkley
 291 velocity profile, in which the velocity field is plug-like above the yield strength [see e.g.,
 292 *Balmforth and Craster, 1999*]. However, inspecting Equation 30, we see that the defor-
 293 mational velocity in the yielded portion diverges like ν^{-n} (see also Figure 4). Removing
 294 this divergence requires that the yield surface Y coincide with the bottom of the glacier,
 295 whence $h |s_x| = T_y$ and $s_x = \pm T_y/h$ and we recover the perfect plastic approximation
 296 [*Nye, 1957; Ultee and Bassis, 2016*]. We now see that when yielded ice flows much more
 297 rapidly than intact ice, the yield strength limits the magnitude of the maximum slope of
 298 the ice sheet.

299 We have now completely determined the velocity field for the case of small horizontal
 300 extensional stresses, but have yet to satisfy the calving front boundary condition. From
 301 Equations 27-28, we see that if τ_{xz} vanishes at the calving front, $\partial_z u_0$ must become $\mathcal{O}(\epsilon^2)$
 302 or smaller and the velocity field becomes plug-like. The velocity field can only become

303 plug-like if deformational velocities are negligible, which requires that, at least near the
 304 calving front, the glacier is intact with stresses less than or equal to the yield strength. An
 305 intact calving front, however, is inconsistent with an active calving margin for grounded
 306 glaciers. The calving front boundary condition can be satisfied for an active calving
 307 margin in two ways. First, it is possible to have a region near the calving front where
 308 the extensional stress becomes large and $\delta\tau_{xx}$ becomes order unity or larger. Second, it
 309 is possible that the stress invariant near the calving front is at the yield strength. We
 310 consider next the case where extensional stresses near the calving front are large (Section
 311 4.3) before examining the more subtle situation when the effective stress at the calving
 312 front is perched at the yield strength (Section 5).

4.3. Large horizontal extensional stresses

313 We next examine the case where there is little resistance to sliding. To this end, we
 314 treat δ as an $\mathcal{O}(1)$ parameter. In this regime, τ_{xz} is $\mathcal{O}(\epsilon)$ smaller than τ_{xx} , but horizontal
 315 gradients in τ_{xx} remain comparable to vertical gradients in τ_{xz} . The effective stress then
 316 becomes $\tau = \delta\epsilon^{-1}|\tau_{xx}|$, with components of deviatoric stress in the unyielded regime:

$$\left. \begin{aligned} \tau_{xx} &= \dot{\gamma}^{1/n-1} u_x \\ \tau_{xz} &= \frac{\delta}{2\epsilon^2} \dot{\gamma}^{1/n-1} u_z \end{aligned} \right\} \tau < T_y, \quad (31)$$

317 and in the yielded regime:

$$\left. \begin{aligned} \tau_{xx} &= \left[(1-\nu) \frac{\epsilon T_y}{\delta \dot{\gamma}} + \nu \dot{\gamma}^{\frac{1}{n}-1} \right] u_x \\ \tau_{xz} &= \left[(1-\nu) \frac{T_y}{\epsilon \dot{\gamma}} + \nu \frac{\delta}{\epsilon^2} \dot{\gamma}^{\frac{1}{n}-1} \right] \frac{1}{2} u_z \end{aligned} \right\} \tau \geq T_y. \quad (32)$$

318 To leading order in Equations 31 and 32, we find $u_z \sim \mathcal{O}(\epsilon^2)$ and weak resistance to sliding
 319 results in plug flow [see, e.g., *Greve and Blatter, 2009*]. This suggests an expansion of the

320 form:

$$u = u_0(x, t) + \epsilon^2 u_2(x, z, t) + \dots \quad (33)$$

321 where we have built in the leading order plug-flow solution and we have again styled
322 indices to reflect the order of terms in the expansion with respect to ϵ .

323 For stresses beneath the yield strength, the analysis parallels the shelfy-stream ap-
324 proximation (SSA) used to model glaciers where most of the resistance originates from a
325 combination of sliding and horizontal stretching [c.f. *Greve and Blatter, 2009*]. Integrat-
326 ing Equation 19a over the depth and applying the surface and basal boundary conditions
327 yields an elliptic equation for velocity,

$$2\delta \frac{\partial}{\partial x} \left(h \left| \frac{\partial u_0}{\partial x} \right|^{1/n-1} \frac{\partial u_0}{\partial x} \right) - \left(\frac{T_b}{|u_0|} + |u_0|^{m-1} \right) u_0 = h \frac{\partial s}{\partial x}, \quad (34)$$

328 equivalent to the usual SSA. The SSA is often used to simulate the rapidly flowing portion
329 of glaciers and ice sheets, but is limited to intact ice.

330 The case where effective stress exceeds the yield strength is more interesting. Assuming
331 T_y remains order unity, we find using Equations 32–33 that the deviatoric stress compo-
332 nents $\tau_{0xx} = \nu |\partial_x u_0|^{1/n-1} \partial_x u_0$ and $\tau_{0xz} = \frac{\nu}{2} \delta |\partial_x u_0|^{1/n-1} \partial_z u_2$ are large compared to the yield
333 strength. Using Equation 20 in Equation 19b and integrating over the glacier thickness
334 results in the momentum equation:

$$2\delta \nu \frac{\partial}{\partial x} \left[h \left| \frac{\partial u_0}{\partial x} \right|^{1/n-1} \frac{\partial u_0}{\partial x} \right] - \left(\frac{T_b}{|u_0|} + |u_0|^{m-1} \right) u_0 = h \frac{\partial s}{\partial x}, \quad (35)$$

335 which can be combined with Equation 22 to find

$$h_t + \frac{\partial(hu_0)}{\partial x} = \dot{a}. \quad (36)$$

336 These equations are analogous to the shelfy-stream approximation [*Greve and Blatter,*
337 *2009*], but this regime corresponds to the flow of disarticulated ice above the yield strength.

Equations 35-36 thus apply to failed ice, and this motion of heavily fractured ice may be analogous to the dynamics of the mixture of failed ice, icebergs and sea ice called *mélange* that clogs many pro-glacial fjords. In this flowline model, however, buttressing from *mélange* could only arise in regions where bed protrusions provided resistance to flow. In more realistic, two-dimensional models, buttressing could also arise from shear stress along fjord margins.

In the limit $\nu \ll 1$, Equation 35 reduces to:

$$-\min\left(\frac{T_b}{|u_0|} + |u_0|^{m-1}, \frac{T_y}{|u_0|}\right)u_0 = h s_x. \quad (37)$$

The minimum arises because, as we saw in section 3.2, the basal shear stress cannot exceed the yield strength of ice in the small ν limit. This regime overlaps with the vertical shear-dominant solution with the $\mathcal{O}(\epsilon^{n+1}/\delta^n)$ vertical shearing term omitted. In the small ν limit, once the bed reaches the yield strength $s_x = \pm T_y/h$ and we again recover the perfect plastic approximation [Nye, 1957]. However, the boundary condition at the calving front can be written in the form:

$$\frac{\partial u_0}{\partial x} = \frac{1}{\delta^n \nu^n} \left[\frac{h}{4} (1 - r^2) - \epsilon(1 - \nu)T_y \right]^n, \quad (38)$$

and we see that with small ν , either $\partial_x u_0$ must diverge or the two terms in square brackets in Equation 38 must balance. Balancing these two terms requires that $\epsilon T_y \sim h(1 - r^2)/4$, which provides a boundary condition on the ice thickness. It is this situation, where the effective stress is at the yield strength, that we examine next.

5. Limiting dynamics: Onset of flow at the yield stress and the perfect plastic approximation

355 Our next goal is to examine the onset of yielding, where the effective stress in the
 356 glacier first approaches the yield strength. Recalling that the yield surface demarks the
 357 boundary between intact and yielded ice, we shall show that in this limiting case the yield
 358 surface is required to extend along the bottom of the glacier *and* through the calving
 359 front, corresponding to the perfect plastic approximation. An important result in this
 360 limit is that the yield condition provides a boundary condition on the ice thickness at the
 361 calving front analogous to one deduced by *Bassis and Walker* [2012].

362 To probe this limiting case, we assume $\nu \ll 1$ (hardness of yielded ice is much smaller
 363 than the hardness of intact ice) and $\epsilon^{1/n+1} \leq \delta \ll 1$, corresponding to a glacier where
 364 sliding is rapid and vertical shear deformation can be neglected—realistic assumptions
 365 near the terminus of many calving glaciers. Anticipating that the flow will be plug-like to
 366 leading order, we pose an expansion of the form:

$$\hat{u} = \frac{1}{\epsilon} \hat{u}_0(x, t) + \hat{u}_1(x, z, t) + \dots, \quad (39)$$

367 where the hat decoration is used to distinguish the expansion in this regime from the
 368 shallow ice and shallow shelf scalings considered previously. We have also built in the
 369 leading-order plug flow solution by explicitly omitting the z dependence of the leading
 370 order \hat{u}_0 term. Moreover, anticipating that flow in the yielded regime is much faster than
 371 flow in the intact regime, we included a leading order term that is inversely proportional
 372 to ϵ to describe the large velocity increase at or above the yield strength. For small ϵ , the
 373 first term $\hat{u}_0(x, t)$ is much larger than $\hat{u}_1(x, z, t)$. Breaking with prior notation, subscripts
 374 labelling the terms in the expansion start at zero to avoid negative indices.

375 With these assumptions, the strain rate invariant is given by

$$\hat{\gamma}_0 = \sqrt{\left(\frac{\partial \hat{u}_0}{\partial x}\right)^2 + \frac{1}{4} \left(\frac{\partial \hat{u}_1}{\partial z}\right)^2}. \quad (40)$$

376 For stresses beneath the yield strength, the rheology can be written:

$$\epsilon^{1/n} \hat{\tau}_{xx} = \hat{\gamma}_0^{1/n-1} \partial_x \hat{u}_0, \quad (41a)$$

$$\frac{\epsilon^{1/n+1}}{\delta} \hat{\tau}_{xz} = \frac{1}{2} \hat{\gamma}_0^{1/n-1} \partial_z \hat{u}_1, \quad (41b)$$

377 and to leading order we find $\partial_x \hat{u}_0 = \partial_z \hat{u}_1 = 0$. In this limit, the strain rates vanish
 378 beneath the yield strength, recovering the ‘rigid-plastic’ limit considered by *Ultee and*
 379 *Bassis* [2016] in which glacier ice passively thickens until the yield strength is reached.

380 Above the yield strength, the rheology can be written

$$\hat{\tau}_{xx} = \left[(1 - \nu) \frac{\epsilon T_y}{\delta \hat{\gamma}_0} + \frac{\nu}{\epsilon^{1/n} \hat{\gamma}_0^{1/n-1}} \right] \frac{\partial \hat{u}_0}{\partial x}, \quad (42a)$$

$$\hat{\tau}_{xz} = \left[(1 - \nu) \frac{T_y}{\hat{\gamma}_0} + \frac{\nu \delta}{\epsilon^{1/n+1} \hat{\gamma}_0^{1/n-1}} \right] \frac{1}{2} \frac{\partial \hat{u}_1}{\partial z}. \quad (42b)$$

381 If $\nu \ll 1$, Equations 42a-42b can be approximated as

$$\hat{\tau}_{xx} = \frac{\epsilon T_y}{\delta \hat{\gamma}_0} \frac{\partial \hat{u}_0}{\partial x}, \quad (43a)$$

$$\hat{\tau}_{xz} = \frac{T_y}{\hat{\gamma}_0} \frac{1}{2} \frac{\partial \hat{u}_1}{\partial z}. \quad (43b)$$

382 Noting that the second stress invariant is

$$\hat{\tau} = \sqrt{\frac{\delta^2}{\epsilon^2} \hat{\tau}_{xx}^2 + \hat{\tau}_{xz}^2} = \frac{T_y}{\hat{\gamma}_0} \sqrt{\left(\frac{\partial \hat{u}_0}{\partial x}\right)^2 + \frac{1}{4} \left(\frac{\partial \hat{u}_1}{\partial z}\right)^2} \equiv T_y, \quad (44)$$

383 we conclude that in the flow regime ‘above’ the yield strength, the stress invariant is, in
 384 fact, perched at the yield strength. Therefore, at the onset of yielding, the effective stress
 385 is at the yield strength through the full ice thickness.

386 To order ϵ we find:

387

$$s_x = \pm \frac{T_y}{h}, \quad (45)$$

388 and we see that this situation corresponds to the perfect plastic approximation. The
389 horizontal velocity is determined by integrating the mass balance equation such that

$$\hat{u}_0 = \epsilon \left(\frac{1}{h(L)} \int_0^{x_L} (\dot{a} - h_t) dx \right), \quad (46)$$

390 and we have now recovered the perfect plastic approximation [Nye, 1957; Ultee and Bassis,
391 2016].

392 Because the effective stress reaches the yield strength throughout the ice thickness,
393 satisfying the calving front boundary condition at $x = L(t)$ requires that the calving front
394 is also a yield surface. The boundary condition defined by Equation 21 is then:

$$\epsilon T_y = \frac{h}{4} \left(1 - \frac{\rho_w d^2}{\rho h^2} \right). \quad (47)$$

395 Consistently enforcing vanishing shear stress at the calving front along with the calving
396 front boundary condition defined by Equation 47 requires that the ice thickness h and
397 vertical shear strain rate $\partial_z \hat{u}_0$ both become order ϵ or smaller and the asymptotic expan-
398 sion breaks order—considered in Appendix A. Nonetheless, we anticipate from Equation
399 47 that requiring the yield surface to extend through the calving front requires

$$h_L = h_y = 2\epsilon T_y + \sqrt{\frac{\rho_w d^2}{\rho} + 4\epsilon^2 T_y^2}, \quad (48)$$

400 where h_y is the *required* terminus thickness and we have discarded the unphysical negative
401 square root.

6. Simple models of calving glaciers

402 In the previous section, we found that the perfect plastic approximation requires the
 403 yield surface demarking the boundary between intact and disarticulated ice to lie along
 404 the bed and the calving front. The assumption that ice is everywhere at the yield strength
 405 is, however, a very restrictive assumption. A less restrictive assumption is that the stress
 406 invariant at the bed must be less than the yield strength of ice. In this case, we use the
 407 rheology of intact ice. Focusing on rapidly sliding glaciers where the internal deforma-
 408 tion of intact ice can be neglected, the dynamics are encompassed by the shelfy-stream
 409 approximation (SSA) defined by Equation 34:

$$2\delta \frac{\partial}{\partial x} \left(h |u_x|^{1/n-1} u_x \right) - \min \left(\frac{T_b}{|u|} + |u|^{m-1}, \frac{T_y}{|u|} \right) u = h s_x. \quad (49)$$

410 In Equation 49, we have dropped the order indices of Equation 34 to ease notation, and
 411 the minimum in the basal shear traction arises because the basal shear stress cannot
 412 exceed the yield strength (section 4.2). With the assumption of intact glacier ice, we also
 413 impose the condition that ice thickness at the terminus $h_L = h(L(t), t)$ not exceed the
 414 yield thickness h_y , resulting in the inequality $h_L \leq h_y$. As we show next, this inequality
 415 serves as a boundary condition and allows us to deduce bounds on the calving rate of
 416 glaciers.

6.1. Bounds on the calving rate: kinematics of calving front evolution

417 Our goal is to derive an expression that describes the rate of terminus advance (or
 418 calving rate) appropriate for a glacier with terminus at—or beneath—the yield thickness.
 419 We start by taking the advective derivative of ice thickness at the terminus:

$$\frac{Dh_L}{Dt} = \frac{\partial h_L}{\partial t} + (u - u_c) \frac{\partial h}{\partial x} \quad (50)$$

where $u - u_c$ denotes the rate of advance of the terminus and u_c is the calving rate (units of length/time) associated with mass lost along the calving front. Next, we use the continuity equation in the form:

$$\frac{\partial h}{\partial t} = \dot{a} - \frac{\partial u}{\partial x} h - \frac{\partial h}{\partial x} u \quad (51)$$

to eliminate $\partial h/\partial t$ from Equation 50, providing a kinematic expression for the ice thickness at the calving front:

$$\frac{Dh_L}{Dt} = \dot{a} - \frac{\partial u}{\partial x} h - \frac{\partial h}{\partial x} u_c. \quad (52)$$

The first term on the right hand side of Equation 52 denotes the accumulation rate at the terminus (often small and/or negative). The second term denotes the rate at which ice thickness decreases at the calving front due to dynamic thinning. The third term is an advective term associated with upstream migration of the calving front due to iceberg calving. Because ice thickness generally increases upstream ($h_x < 0$), the advective term usually acts to increase ice thickness at the calving front. Provided $h_x < 0$, the calving rate u_c changes the balance between dynamic thinning and advective thickening at the calving front, controlling whether the terminus thins or thickens. Equation 52, however, is a purely kinematic description and does not provide a means of specifying the calving rate u_c . To specify the calving rate, we must apply additional constraints.

6.2. Bounds on the calving rate: Yield thickness greater than flotation thickness

Icebergs detach from calving glaciers and this suggests that the stress invariant at the terminus of actively calving glaciers must be perched near the yield strength. Equation 48 translates this requirement to a constraint on ice thickness. Moreover, for grounded glaciers, the ice thickness also cannot be less than the flotation thickness $h_f = \rho_w d/\rho$.

439 Provided $h_f \leq h_y$, the terminus thickness is bounded above and below and $h_f \leq h_L \leq h_y$.

440 We treat the case $h_f > h_y$ in the next section.

441 Considering first glaciers with a calving front thickness perched at the yield thickness,
442 we take the advective derivative of the yield thickness:

$$\frac{Dh_y}{Dt} = (u - u_c) \frac{\partial h_y}{\partial x}, \quad (53)$$

443 and equate it to the advective derivative of ice thickness at the terminus defined by
444 Equation 52, where we have also assumed that the bed topography is fixed (or evolves
445 slowly enough that the time derivative of the yield thickness h_y can be neglected). This
446 allows us to uniquely determine the calving rate necessary to maintain the terminus at
447 the yield thickness:

$$u_c = u_y = u - \frac{\dot{a} - u \frac{\partial h}{\partial x} - h \frac{\partial u}{\partial x}}{\left(\frac{\partial h_y}{\partial x} - \frac{\partial h}{\partial x} \right)}, \quad \text{when } h_L = h_y, \quad (54)$$

448 where we have assumed $(\partial_x h_y - \partial_x h) \neq 0$ and u_y denotes the specific calving rate u_c
449 required to maintain the ice thickness at the yield thickness h_y .

450 A similar calculation shows that if the ice thickness is required to remain at flotation,
451 then the calving rate u_f necessary to maintain the calving front at buoyancy is given by:

$$u_c = u_f = u - \frac{\dot{a} - u \frac{\partial h}{\partial x} - h \frac{\partial u}{\partial x}}{\left(\frac{\partial h_f}{\partial x} - \frac{\partial h}{\partial x} \right)}, \quad \text{when } h_L = h_f. \quad (55)$$

452 Note that $\dot{x}_g = u - u_f$ is just the usual expression for grounding line migration [*Schoof*,
453 2007]. However, the physical interpretation of Equation 55 is that the calving front
454 advances and thins to buoyancy before calving, analogous to the buoyant calving regime
455 proposed for Helheim Glacier [e.g., *Murray et al.*, 2015].

From Equation 52, if the ice thickness is initially less than the yield thickness and the calving rate u_c is larger than u_y , then the ice thickness will increase until the yield strength is reached and Equation 54 will become valid again. Hence, Equation 54 bounds the long-term calving rate from above. Similarly, if the ice thickness is initially greater than the flotation thickness and the calving rate u_c is smaller than u_f , then the ice thickness will decrease until the flotation thickness is reached and Equation 55 will become valid. Hence, Equation 55 bounds the calving rate from below.

Formally Equation 54 is an *upper* bound and Equation 55 is a *lower* bound on calving rate when $\partial_x h_Y - \partial_x h > 0$ (i.e., when ice thickness decreases toward the terminus and bed topography varies on a length scale that is large compared with ice thickness—see Appendix A). When $\partial_x h_Y - \partial_x h < 0$, the bounds are reversed.

At the onset of yielding, continuity of strain rate across the yield surface at the calving front requires:

$$\frac{\partial u}{\partial x} = \frac{1}{\delta^n} \left[\frac{1}{4} h (1 - r^2) \right]^n. \quad (56)$$

So long as the ice thickness is known and we have a model capable of calculating the velocity at the terminus u , Equations 54-56 provide a self-consistent means of estimating the calving rate (or rates of terminus advance). Together, these two limits suggest that long term calving rates are constrained by the fact that the ice thickness must remain less than the yield thickness and greater than the flotation thickness. These bounds remain valid until the flotation thickness exceeds the yield thickness, which we consider next.

6.3. Bounds on the calving rate: Yield thickness less than flotation thickness

For glaciers on retrograde beds, such as Pine Island and Thwaites glaciers grounded deep below sea level, retreat of the calving front will eventually result in an ice thickness

477 where the flotation thickness exceeds the yield thickness of ice [*Bassis and Walker, 2012*].
 478 In these cases, we must use Equation 35 to compute the velocity u for the portions of
 479 the glacier that are yielded. We can still use Equation 55 to compute the calving rate
 480 associated with migration of the fully yielded terminus, which must now be at the flotation
 481 thickness. However, we must use the yielded rheology in computing the horizontal strain
 482 rate:

$$\frac{\partial u}{\partial x} = \frac{1}{\nu^n \delta^n} \left[\frac{1}{4} h (1 - r^2) \right]^n. \quad (57)$$

483 Both the velocity and grounding line dynamics now depend on the viscosity of yielded
 484 ice via the hardness ratio ν . Despite poor constraints on the precise value of ν , in the
 485 plausible case that yielded ice is softer than intact ice ($\nu \ll 1$) and in the absence of
 486 stabilizing features, dynamic thinning and grounding line retreat in this regime could occur
 487 as catastrophic disintegration—perhaps analogous to the disintegration of the Larsen B
 488 ice shelf [e.g., *Scambos et al., 2000*]. In our model, however, rapid disintegration could
 489 occur for grounded portions of the ice sheet. Even for modest values of ν , we anticipate
 490 retreat could occur much more rapidly than would be simulated by models that assume
 491 Glen’s flow law holds across all stress regimes. This potential progression of failure in
 492 deep retrograde beds is illustrated schematically in Figure 5.

7. Numerical Examples

7.1. Four reduced models of calving glaciers

493 Equations 45-49 and Equations 54-56 provide a complete set of equations that specifies
 494 glacier evolution and terminus position. We illustrate the application of these equations
 495 for four limiting cases. The first model, which we call the ‘Weertman’ model, corresponds

496 to Equation 49 with the basal yield strength $T_b = 0$, resulting in the dynamic equation:

$$2\delta \frac{\partial}{\partial x} \left(h |u_x|^{1/n-1} u_x \right) - \min \left(|u|^{m-1}, \frac{T_y}{|u|} \right) u = h s_x. \quad (58)$$

497 The second model, which we call the Plastic bed model, assumes $T_y \gg T_b$ and hence the
498 shear stress at the bed is equal to the yield strength of ice everywhere, resulting in the
499 dynamic equation:

$$2\delta \frac{\partial}{\partial x} \left(h |u_x|^{1/n-1} u_x \right) - \frac{T_y}{|u|} u = h s_x. \quad (59)$$

500 These two models reduce further if $\delta \ll 1$. Our third model, which we call the SIA
501 model, corresponds to $\delta \ll 1$ in the Weertman model. Dropping the term related to
502 the longitudinal stress gradient and combining with the ice thickness evolution equation
503 provides the usual SIA diffusive equation for the glacier surface elevation:

$$h_t = \left(h^{1/m+1} |s_x|^{1/m-1} s_x \right)_x + \dot{a}, \quad |s_x| \leq \frac{T_y}{h}. \quad (60)$$

504 Our fourth model corresponds to $\delta \ll 1$ in the ‘Plastic bed’ model and reduces to the
505 Perfect plastic approximation:

$$s_x = \pm \frac{T_y}{h}, \quad u = \epsilon \left(\frac{1}{h(L)} \int_0^{x_L} (\dot{a} - h_t) dx \right). \quad (61)$$

506 For a discussion of numerical methods, we refer the reader to Appendix B.

7.2. Geometric setting

507 We applied the calving parameterization defined by Equation 54 to an idealized geom-
508 etry motivated by *Oerlemans* [2008]. The idealized glacial geometry assumes a glacier on
509 a gently sloping bed with a Gaussian bump, representing a sill. In dimensional units, the
510 bed takes the form:

$$b(x) = b_0 - \alpha x + b_1 \exp \left[- \left(\frac{x - x_0}{\sigma} \right)^2 \right]. \quad (62)$$

Parameters follow *Oerlemans* [2008] and are provided in Table 1 in dimensional form.

7.3. Glacier profiles

We first considered the temporal evolution of glaciers, including advance and retreat of the calving front. We assumed a slowly changing accumulation rate \dot{a} of the form

$$\dot{a} = a_0 + \Delta a \sin\left(\frac{2\pi t}{T}\right). \quad (63)$$

In all calculations we assumed ice at the terminus is at the yield strength and evolved the terminus according to Equation 54. Figure 6 shows a sequence of snapshots illustrating glacier profiles constructed using the Perfect plastic approximation and Plastic bed model. For a given terminus position, differences between the Perfect plastic and Plastic bed profiles are largest upstream, away from the calving front. This pattern is a consequence of the Perfect plastic approximation neglecting deformation near the ice divide, requiring a larger slope and producing a thicker glacier. Figure 7 shows an equivalent set of snapshots, but this time comparing the Weertman model with the simpler boundary layer approximation defined by the SIA model. For the parameter regime used here, longitudinal stresses are small everywhere except near the calving front and the profiles are in close agreement. Differences between profiles are greatest early on when the glaciers are relatively small and deformational creep cannot be neglected.

Figure 8 shows a time series of glacier length, calving rate and terminus velocity as the accumulation rate changes computed for (1) the Perfect plastic, (2) Plastic bed and (3) Weertman models. (We omit the SIA model because the difference with the Weertman model is small.) Despite the slowly varying forcing, all three models exhibit sudden changes in terminus position that manifest as “spikes”, analogous to the sudden retreat

531 of real glaciers. In this case, the glacier responds slowly when its terminus is perched on a
532 stable position on the sill. Retreat occurs rapidly when the glacier retreats (or advances)
533 into an overdeepening, where ice thickness (and flux) rapidly increase. This is analogous
534 to observations of rapid retreat when the bed is deep [e.g., *Benn et al.*, 2007]. The Plastic
535 bed, Perfect plastic and Weertman models predict advance rates and retreat rates that
536 are broadly similar. However, the Plastic bed and Perfect plastic models are more stable
537 to changes in accumulation rate and have a delayed retreat compared to the Weertman
538 model.

7.4. Multiple steady state and hysteresis

539 Observations show that advance and retreat of tidewater glaciers can exhibit complex
540 patterns that are not clearly synced with climate forcing [e.g., *Pfeffer*, 2003]. To assess
541 the ability of our suite of models to simulate a highly non-linear response to climate,
542 we computed stable steady-state terminus positions for the forcing previously considered.
543 Figure 9 shows bifurcation diagrams illustrating stable and unstable terminus positions as
544 a function of accumulation rate \dot{a} . We find 3 bifurcation points, with the first bifurcation
545 point located near the coastline where the glacier first comes into contact with the ocean.
546 The second and third bifurcation points occur at the deepest part of the overdeeping and
547 the top of the sill, respectively. The positions of these bifurcation points are determined by
548 the geometry of the glacier bed. Different sliding laws and choices of yield strength result
549 in identical bifurcation points along the bed. This suggests that bed geometry controls the
550 stable positions in which we observe glaciers. However, the sliding law controls climate
551 sensitivity and the rates of retreat and advance.

8. Discussion

552 The thin film plastic approximation for glaciers developed here provides an avenue to
553 simulate intact and fractured ice in a single modeling framework. Assuming that (i)
554 the bi-viscous rheology of ice approximates real glacier flow, (ii) yielded ice flows much
555 faster than intact ice, and (iii) the calving front is the boundary separating yielded from
556 unyielded ice, we can bound the long term calving rate and calving flux. This bound is
557 independent of the rheology of failed ice provided the yield thickness remains less than the
558 flotation thickness. However, once a glacier retreats into an over-deepening bed where the
559 flotation thickness exceeds the yield thickness, grounding line retreat will be paced by the
560 rheology of the yielded ice mélange. Mélange rheology is poorly constrained [e.g., *Robel*,
561 2017], but it is likely much weaker than intact ice. Weak mélange opens the potential
562 for ice sheet disintegration that proceeds much more rapidly than is possible with fully
563 intact ice—a consequence already deduced by *Weertman* [1974] in his original treatment
564 of the marine ice sheet instability. The mechanical simplifications we adopted do neglect
565 bending and buckling stresses, which could be important near the calving front of glaciers.
566 A more detailed treatment in the future may seek to include these effects—especially as
567 glaciers approach buoyancy.

568 The idealized simulations that we conducted also display qualitatively realistic responses
569 to climate forcing—including multiple steady states. Crucially, for the entire suite of
570 glacier dynamics models considered, stable terminus positions are controlled by bed ge-
571 ometry. Near the most advanced position, we found that glaciers can exhibit remarkably
572 little sensitivity to changes in climate forcing. However, once the climate forcing reaches
573 a tipping point, retreat is irreversible unless the accumulation rate becomes significantly

574 more positive. Although these results depend on the idealized geometry we assumed,
575 most tidewater glaciers have a geometry that includes an over-deepening and sill. Thus,
576 our results likely apply to more realistic geometries and may help explain the markedly
577 different sensitivity of adjacent glaciers to changes in climate forcing.

578 Our model, although simplified, builds on the recently proposed marine ice cliff instabil-
579 ity [*Bassis and Walker, 2012; DeConto and Pollard, 2016*]. At least for two dimensions,
580 where the maximum shear stress is equal to the effective stress, the bound on ice thickness
581 we derived is identical to that proposed by *Bassis and Walker [2012]*, with a factor of two
582 error in *Bassis and Walker [2012]* corrected. However, unlike *Bassis and Walker [2012]*,
583 which only provides a threshold on the maximum ice thickness permissible, our model is
584 able to relate the ice thickness threshold to the rate of retreat possible associated with the
585 marine ice cliff instability. These bounds emerge from the assumption that the effective
586 stress at the terminus must always be less than the yield strength of ice and only depend
587 on a single parameter—the yield strength of ice. This should be contrasted with empir-
588 ical calving law proposed by *DeConto and Pollard [2016]* that is based on retreat rates
589 for Jakobshavn Isbræ and calibrated to match paleo ice sheet extents. Furthermore, our
590 bound for retreat rates depends on the near-terminus geometry (ice thickness, bed slope
591 and ice thickness gradient), accumulation rate and hardness of ice. A consequence is that
592 our model predicts that glaciers with identical thickness may retreat at markedly different
593 rates, depending on the geometric setting and climate forcing. This may help explain the
594 observed breakdown in correlations between ice thickness and calving rates during glacier
595 retreat [*Van Der Veen, 1996*] and agrees with observational evidence that geometry plays
596 a dominant role in controlling calving rates [*Catania et al., 2018; Enderlin et al., 2018*].

597 Teasing out if our bound on calving rate holds for more realistic situations, however,
598 requires a more thorough comparison of model predictions with observations using real-
599 istic geometry and forcing. We previously used a model similar to the SIA-limit of the
600 more general model developed here to successfully reproduce characteristics of Heinrich
601 Events [*Bassis et al.*, 2017], but this earlier study was highly idealized. Applying our
602 model formalism to more realistic modern glacier configurations along with developing
603 approximations that apply to two-dimensional (plan view) and fully three-dimensional
604 models is a focus of current work.

9. Conclusions

605 We have developed a thin film viscoplastic model that encapsulates the flow of intact
606 and yielded ice. Requiring that the effective stress within a glacier is bounded from above
607 by the yield strength provides an upper bound on the ice thickness at the calving front
608 (Equation 47). Remarkably, a bound on the long term average rate of terminus advance
609 emerges naturally as a consequence of the assumption that glacier ice cannot exceed
610 the yield thickness (Equation 52). This approach differs from the current trends in ice
611 dynamics in which the ‘fluid’ part of dynamics is treated independently of the ‘fracture’
612 component. In our model, the evolution equation for terminus position emerges from
613 the bi-viscous rheology as opposed to being imposed separately. This bi-viscous rheology
614 provides a promising avenue to simulate the failure of glacier ice.

615 The calving rate evolution equation we derived provides a bound on calving fluxes and
616 depends on a single additional parameter—the yield strength. Promisingly, the yield
617 strength is a material property that can be constrained by field and laboratory measure-
618 ments [e.g., *Vaughan*, 1993; *Bassis and Walker*, 2012]. Furthermore, our model provides

619 a simple theoretical framework to study the rapid retreat rates that recent studies [*Bassis*
620 *and Walker*, 2012; *DeConto and Pollard*, 2016; *Bassis et al.*, 2017] suggest may affect the
621 West Antarctic Ice Sheet under calving cliff collapse.

Appendix A. Extensional stress boundary layer in the perfect plastic approximation

622 We return to the perfect plastic approximation continuing with the expansion and nota-
623 tion defined in section 5. Requiring a dominant balance between gradients in longitudinal
624 stress and sliding when ice is at the yield strength at the bed suggests the rescaling:

$$x - x_c = \epsilon^2 X, \quad s = \epsilon S, \quad h = \epsilon H, \quad b = \epsilon B, \quad \hat{u} = \epsilon^{-1} U. \quad (64)$$

625 Following *Schoof* [2007], we also assume that the bed topography B only varies sig-
626 nificantly on the ‘outer’ length scale associated with the original horizontal coordinate
627 x . With this rescaling, the strain rate components in the boundary layer become:
628 $\hat{u}_x = \epsilon^{-3} U_X$, $\hat{u}_z = \epsilon^{-2} U_Z$, which motivates the strain rate invariant rescaling

$$\hat{\gamma} = \epsilon^{-3} E = \epsilon^{-3} \sqrt{U_X^2 + U_Z^2}. \quad (65)$$

629 Assuming an expansion of the form $\hat{U} = \hat{U}_0(X, t) + \epsilon^2 \hat{U}_2(X, Z, t) + \dots$ the leading order
630 stress balance becomes

$$2 \left(HT_y \frac{\partial_X \hat{U}_0}{|\partial_X \hat{U}_0|} \right)_X - T_y \frac{\hat{U}_0}{|\hat{U}_0|} = HH_X, \quad (66)$$

631 whereas the ice thickness evolution equation to order ϵ becomes

$$(H\hat{U}_0)_X = 0. \quad (67)$$

632 Our boundary condition that vertical shear stress vanish at $X = 0$ is now automatically
633 satisfied, and the boundary condition on longitudinal stress becomes an ice thickness

634 boundary condition:

$$T_y = \frac{H}{4} \left(1 - \frac{\rho_w D^2}{\rho H^2} \right). \quad (68)$$

635 This equation can only be satisfied if the ice thickness at the calving front $H_c = H(0, t)$
636 is given by:

$$H_c = H_y = 2T_y + \sqrt{\frac{\rho_w D^2}{\rho} + 4T_y^2} \quad (69)$$

637 where H_y is the *required* terminus thickness so the glacier is at the yield strength and we
638 have discarded the unphysical negative square root.

639 Using the boundary condition on ice thickness at the terminus given by Equation 69,
640 Equation 66 now can be explicitly integrated to find an expression for ice thickness in the
641 boundary layer:

$$H = 2T_y + \sqrt{4T_y^2 + \frac{\rho_w}{\rho} D^2 - 2T_y X}, \quad -\infty < X \leq 0. \quad (70)$$

642 In the limit $X \rightarrow -\infty$, $H \sim \sqrt{-2T_y X}$, matching equation 45 for ice thickness in the
643 limit that the bed is flat. The flat bed condition, however, is exactly what we deduced
644 is required in the boundary layer so long as bed topography varies on the ‘outer’ length
645 scale and the solutions match in the limit $x \rightarrow \infty$ and $X \rightarrow -\infty$.

Appendix B. Model numerics

646 For the SSA type models, we impose a symmetric boundary condition at the ice divide
647 $s_x = 0$ and $u = 0$ at $x = 0$. For the SIA type models we need to impose $s_x = 0$ at $x = 0$.
648 For the perfect plastic model we need only specify the thickness at the terminus. To
649 accurately resolve the terminus position, we adopt a moving grid. If the terminus position
650 is located at $x_c(t)$, then defining

$$\xi = \frac{x}{x_c}, \quad \tilde{t} = t, \quad (71)$$

651 maps the interval $0 \leq x \leq x_c(t)$ into the interval $0 \leq \xi \leq 1$. The variable \tilde{t} is introduced to
 652 distinguish between partial derivatives obtained holding x or ξ constant. Straightforward
 653 application of the chain rule then leads to

$$\frac{\partial}{\partial x} = \frac{1}{x_c} \frac{\partial}{\partial \xi} \quad (72)$$

$$\frac{\partial}{\partial t} = \frac{\partial}{\partial \tilde{t}} - \frac{\xi}{x_c} \frac{dx_c}{d\tilde{t}} \frac{\partial}{\partial \xi}. \quad (73)$$

654 These transformations apply to all equations. To accurately resolve the boundary layer
 655 near the calving front, we use an unevenly spaced grid with points in the interval $[-1, 1]$
 656 given by $\xi_j = 0.5 \cos(j\pi/N) + 0.5$ where N is the number of grid points and $0 \leq j \leq N$.
 657 The irregular grid spacing is accommodated using a finite element formulation with a
 658 basis set of ‘tent’ functions that are defined to be unity at a single node and to vary
 659 linearly between nodes. To avoid numerical artifacts or resolution issues, we set $N=1600$
 660 or higher.

661 **Acknowledgments.** This work was supported by National Science Foundation grant
 662 ANT 114085, National Oceanic and Atmospheric Administration, Climate Process Team:
 663 Iceberg Calving grant NA13OAR4310096 and National Science Foundation grant PLR-
 664 131568. No data was used in this study. Code used to generate results is available at
 665 <https://github.com/jbassis/pyglacier.git>. The authors would like to thank the editor,
 666 Bryn Hubbard along with two anonymous reviewers.

References

667 Albrecht, T., and A. Levermann, Fracture field for large-scale ice dynamics, *Journal of*
 668 *Glaciology*, 58(207), 165–176, doi:10.3189/2012JoG11J191, 2012.

- 669 Astrom, J. A., et al., Termini of calving glaciers as self-organized critical systems, *Nature*
670 *Geosci*, 7(12), 874–878, doi:10.1038/NGEO2290, 2014.
- 671 Balmforth, N. J., and R. V. Craster, A consistent thin-layer theory for Bingham plas-
672 tics, *Journal of Non-Newtonian Fluid Mechanics*, 84(1), 65–81, doi:10.1016/S0377-
673 0257(98)00133-5, 1999.
- 674 Bassis, J. N., The statistical physics of iceberg calving and the emergence of universal
675 calving laws, *Journal of Glaciology*, 57(201), 3–16, doi:10.3189/002214311795306745,
676 2011.
- 677 Bassis, J. N., and S. S. Jacobs, Diverse calving patterns linked to glacier geometry, *Nature*
678 *Geoscience*, 6(10), 833–836, doi:10.1038/NGEO1887, 2013.
- 679 Bassis, J. N., and Y. Ma, Evolution of basal crevasses links ice shelf stabil-
680 ity to ocean forcing, *Earth and Planetary Science Letters*, 409, 203 – 211, doi:
681 <http://dx.doi.org/10.1016/j.epsl.2014.11.003>, 2015.
- 682 Bassis, J. N., and C. C. Walker, Upper and lower limits on the stability of calving glaciers
683 from the yield strength envelope of ice, *Proceedings of the Royal Society A: Mathemati-
684 cal, Physical and Engineering Science*, 468(2140), 913–931, doi:10.1098/rspa.2011.0422,
685 2012.
- 686 Bassis, J. N., S. V. Petersen, and L. M. Cathles, Heinrich events triggered by ocean forcing
687 and modulated by isostatic adjustment, *Nature*, 542, 332–334, doi:10.1038/nature21069,
688 2017.
- 689 Benn, D. I., C. R. Warren, and R. H. Mottram, Calving processes and the
690 dynamics of calving glaciers, *Earth-Science Reviews*, 82(3-4), 143–179, doi:
691 10.1016/j.earscirev.2007.02.002, 2007.

- 692 Borstad, C., A. Khazendar, and E. Larour, A damage mechanics assessment of the Larsen
693 B ice shelf prior to collapse: Toward a physically-based calving law, *Geophysical Re-*
694 *search Letters*, 39(18), L11,604, doi:10.1029/2012GL053317, 2012a.
- 695 Borstad, C., A. Khazendar, B. Scheuchl, M. Morlighem, E. Larour, and E. Rignot, A
696 constitutive framework for predicting weakening and reduced buttressing of ice shelves
697 based on observations of the progressive deterioration of the remnant Larsen B Ice Shelf,
698 *Geophysical Research Letters*, 43(5), 2027–2035, doi:10.1002/2015GL067365, 2016.
- 699 Borstad, C. P., A. Khazendar, E. Larour, M. Morlighem, E. Rignot, M. P. Schodlok, and
700 H. Seroussi, A damage mechanics assessment of the Larsen B ice shelf prior to collapse:
701 Toward a physically-based calving law, *Geophysical Research Letters*, 39(18), L18,502,
702 doi:10.1029/2012GL053317, 2012b.
- 703 Catania, G. A., L. A. Stearns, D. A. Sutherland, M. J. Fried, T. C. Bartholomaus,
704 M. Morlighem, E. Shroyer, and J. Nash, Geometric Controls on Tidewater Glacier Re-
705 treat in Central Western Greenland, *Journal of Geophysical Research: Earth Surface*,
706 123(8), 2024–2038, doi:10.1029/2017JF004499, 2018.
- 707 Cuffey, K., and W. S. B. Paterson, *The Physics of Glaciers*, third ed., Reed Educational
708 and Professional Publishing Ltd, Oxford, 1994.
- 709 Dahlen, F. A., Critical taper model of fold-and-thrust belts and accretionary
710 wedges, *Annual Review of Earth and Planetary Sciences*, 18(1), 55–99, doi:
711 10.1146/annurev.ea.18.050190.000415, 1990.
- 712 DeConto, R. M., and D. Pollard, Contribution of Antarctica to past and future sea-level
713 rise, *Nature*, 531(7596), 591–597, doi:10.1038/nature17145, 2016.

- 714 Duddu, R., J. N. Bassis, and H. Waisman, A numerical investigation of surface crevasse
715 propagation in glaciers using nonlocal continuum damage mechanics, *Geophysical Re-*
716 *search Letters*, *40*(12), 3064–3068, doi:10.1002/grl.50602, 2013.
- 717 Enderlin, E. M., S. O’Neel, T. C. Bartholomaus, and I. Joughin, Evolving Environmental
718 and Geometric Controls on Columbia Glacier’s Continued Retreat, *Journal of Geophys-*
719 *ical Research: Earth Surface*, *123*(7), 1528–1545, doi:10.1029/2017JF004541, 2018.
- 720 Greve, R., and H. Blatter, *Dynamics of ice sheets and glaciers*, Springer, doi:10.1007/978-
721 3-642-03415-2, 2009.
- 722 Howat, I. M., I. Joughin, S. Tulaczyk, and S. P. Gogineni, Rapid retreat and acceleration
723 of Helheim Glacier, East Greenland, *Geophysical Research Letters*, *32*(22), L22,502,
724 doi:10.1029/2005GL024737, 2005.
- 725 Howat, I. M., I. Joughin, and T. A. Scambos, Rapid changes in ice discharge from Green-
726 land outlet glaciers, *Science*, *315*(5818), 1559–1561, doi:10.1126/science.1138478, 2007.
- 727 Joughin, I., I. Howat, R. B. Alley, G. Ekstrom, M. Fahnestock, T. Moon, M. Nettles,
728 M. Truffer, and V. C. Tsai, Ice-front variation and tidewater behavior on Helheim
729 and Kangerdlugssuaq Glaciers, Greenland, *Journal of Geophysical Research*, *113*(F1),
730 F01,004, doi:10.1029/2007JF000837, 2008.
- 731 Krimmel, R. M., Photogrammetric data set, 1957-2000, and bathymetric measurements
732 for Columbia Glacier, Alaska, *Tech. rep.*, USGS, 2001.
- 733 McFadden, E. M., I. M. Howat, I. Joughin, B. E. Smith, and Y. Ahn, Changes in the
734 dynamics of marine terminating outlet glaciers in west Greenland (2000–2009), *Journal*
735 *of Geophysical Research*, *116*(F2), F02,022, doi:10.1029/2010JF001757, 2011.

- 736 McNabb, R. W., et al., Using surface velocities to calculate ice thickness and bed topog-
737 raphy: A case study at Columbia Glacier, Alaska, USA, *Journal of Glaciology*, 58(212),
738 1151–1164, doi:10.3189/2012JoG11J249, 2012.
- 739 Meier, M. F., and A. Post, Fast tidewater glaciers, *Journal of Geophysical Research*,
740 92(B9), 9051–9058, doi:10.1029/JB092iB09p09051, 1987.
- 741 Moresi, L., F. Dufour, and H. B. Mühlhaus, A Lagrangian integration point finite ele-
742 ment method for large deformation modeling of viscoelastic geomaterials, *Journal of*
743 *computational physics*, 184(2), 476–497, doi:10.1016/S0021-9991(02)00031-1, 2003.
- 744 Murray, T., et al., Dynamics of glacier calving at the ungrounded margin of Helheim
745 Glacier, southeast Greenland, *Journal of Geophysical Research: Earth Surface*, 120(6),
746 964–982, doi:10.1002/2015JF003531, 2015.
- 747 Nick, F. M., C. J. Van der Veen, A. Vieli, and D. I. Benn, A physically based calving model
748 applied to marine outlet glaciers and implications for the glacier dynamics, *Journal of*
749 *Glaciology*, 56(199), 781–794, doi:10.3189/002214310794457344, 2010.
- 750 Nye, J. F., The distribution of stress and velocity in glaciers and ice-sheets, *Proceedings of*
751 *the Royal Society of London. Series A, Mathematical and Physical Sciences*, 239(1216),
752 113–133, doi:10.1098/rspa.1957.0026, 1957.
- 753 Oerlemans, J., *Minimal glacier models*, Igitur, Universiteitsbibliotheek Utrecht, 2008.
- 754 O’Neel, S., W. T. Pfeffer, R. Krimmel, and M. Meier, Evolving force balance at Columbia
755 Glacier, Alaska, during its rapid retreat, *Journal of Geophysical Research*, 110(F3),
756 F03,012, doi:10.1029/2005JF000292, 2005.
- 757 O’Neill, C., L. Moresi, D. Müller, R. Albert, and F. Dufour, Ellipsis 3D: A particle-in-cell
758 finite-element hybrid code for modelling mantle convection and lithospheric deforma-

- 759 tion, *Computers & Geosciences*, *32*(10), 1769–1779, doi:10.1016/j.cageo.2006.04.006,
760 2006.
- 761 Pfeffer, W. T., Tidewater glaciers move at their own pace, *Nature*, *426*(6967), 602, doi:
762 10.1038/426602b, 2003.
- 763 Pralong, A., and M. Funk, Dynamic damage model of crevasse opening and appli-
764 cation to glacier calving, *Journal of Geophysical Research*, *110*(B1), B01,309, doi:
765 10.1029/2004JB003104, 2005.
- 766 Rignot, E., I. Velicogna, M. R. van den Broeke, A. Monaghan, and J. T. M. Lenaerts,
767 Acceleration of the contribution of the Greenland and Antarctic ice sheets to sea level
768 rise, *Geophysical Research Letters*, *38*(5), L05,503, doi:10.1029/2011GL046583, 2011.
- 769 Rist, M. A., P. R. Sammonds, H. Oerter, and C. S. M. Doake, Fracture of Antarctic shelf
770 ice, *Journal of Geophysical Research*, *107*(B1), 2002–2002, doi:10.1029/2000JB000058,
771 2002.
- 772 Robel, A. A., Thinning sea ice weakens buttressing force of iceberg mélange and promotes
773 calving, *Nature Communications*, *8*, 14,596, doi:10.1038/ncomms14596, 2017.
- 774 Scambos, T. A., C. Hulbe, M. Fahnestock, and J. Bohlander, The link between climate
775 warming and break-up of ice shelves in the Antarctic Peninsula, *Journal of Glaciology*,
776 *46*, 516–530, doi:10.3189/172756500781833043, 2000.
- 777 Schoof, C., Marine ice-sheet dynamics. Part 1. The case of rapid sliding, *Journal of Fluid*
778 *Mechanics*, *573*, 27–55, doi:10.1017/S0022112006003570, 2007.
- 779 Schulson, E. M., Brittle failure of ice, *Engineering Fracture Mechancis*, *68*(17), 1839–1887,
780 doi:10.1016/S0013-7944(01)00037-6, 2001.

- 781 Schulson, E. M., and P. Duval, *Creep and fracture of ice*, Cambridge University Press,
782 doi:10.3189/S0022143000206254, 2009.
- 783 Straneo, F., et al., Challenges to understanding the dynamic response of Greenland's ma-
784 rine terminating glaciers to oceanic and atmospheric forcing, *Bulletin of the American*
785 *Meteorological Society*, 94(8), 1131–1144, doi:10.1175/BAMS-D-12-00100.1, 2013.
- 786 Thomas, R., Calving bay dynamics and ice sheet retreat up the St. Lawrence Valley
787 system, *Géographie physique et Quaternaire*, 31(3-4), 347–356, doi:10.7202/1000282ar,
788 1977.
- 789 Ultee, L., and J. Bassis, The future is Nye: an extension of the perfect plastic ap-
790 proximation to tidewater glaciers, *Journal of Glaciology*, 62(236), 1143–1152, doi:
791 10.1017/jog.2016.108, 2016.
- 792 Van Der Veen, C. J., Tidewater calving, *Journal of Glaciology*, 42(141), 375385, doi:
793 10.3189/S0022143000004226, 1996.
- 794 Van der Veen, C. J., *Fundamentals of glacier dynamics*, Balkema, 1999.
- 795 Vaughan, D. G., Relating the occurrence of crevasses to surface strain rates, *Journal of*
796 *Glaciology*, 39(132), 255266, doi:10.3189/S0022143000015926, 1993.
- 797 Weertman, J., Stability of the junction of an ice sheet and an ice shelf, *Journal of Glaciol-*
798 *ogy*, 13(67), 3–11, doi:10.3189/S0022143000023327, 1974.
- 799 Weertman, J., Bottom crevasses, *Journal of Glaciology*, 25(91), 185188, doi:
800 10.3189/S0022143000010418, 1980.

Figure 1. Sketch showing the coordinate system and geometry assumed. A yield surface $Y(x)$ is also shown which is initially quasi-parallel to the bed, but rises and connects with the surface near the calving front.

Figure 2. Diagram illustrating the bi-viscous rheology for various values of the ratio of hardness of intact and yielded ice. When the ratio $B_f/B_i = 1$, yielded ice has the same effective viscosity as intact ice, and power-law creep continues at the same rate above the yield strength. When the ratio $B_f/B_i < 1$, there is an abrupt transition at the yield strength to a smaller ice hardness that results in a smaller increase in effective stress for a given increase in effective strain rate. As the ratio B_f/B_i approaches zero, ice behaves like a power-law creeping material up until the yield strength, τ_y , at which point the effective stress can no longer increase and ice behaves like a plastic material.

Figure 3. Schematic illustrating the boundary between intact and yielded ice. Panel (a) shows an initial condition that consists of intact and yielded ice separated by a yield surface denoted by $Y(x)$. Panel (b) shows deformation of yielded ice concentrated along fractures and faults forming a yielded ice mélange. The yielded rheology simulates the bulk effect of fractures and bergs, conceptually illustrated with the dashed line in Panel (b). Panel (c) shows the end state after the yielded plug of mélange has rapidly deformed and been exported away exposing the yield surface as the calving front. The transition from Panel (a) to Panel (b) is paced by the characteristic time of the system and occurs nearly-instantaneously if yielded ice deforms much faster than intact ice.

Figure 4. Illustration of the velocity profile above and below the yield surface Y as a function of the ratio of the hardness parameter of yielded to intact ice ν . When $\nu = 1$, velocity follows the usual SIA profile of creeping above and below the yield surface. As ν becomes smaller, the weaker rheology of yielded ice results in rapidly increasing velocities in the yielded layer.

Figure 5. Conceptual illustration of the evolution of a glacier. Starting at the most advanced position (time t_0 , light gray shaded profile), thinning of the glacier decreases the ice thickness. As the ice thickness at the terminus decreases, the calving front retreats to a position where the thickness can again reach the yield thickness (time t_2 medium shaded gray profile). If the glacier retreats into a deep trough, then the buoyancy thickness may exceed the yield thickness (illustrated with a dashed red line). In this case, the yielded rheology will result in rapid thinning (with the yielded rheology, Equation 35), a (nearly) instantaneous retreat of the grounding line to a position where the yield thickness can again be reached and formation of a floating melange tongue (t_2 , dark gray shaded profile).

Quantity	value	description
τ_y	150 kPa	yield strength
B_i	$10^8 \text{ Pa s}^{-1/3}$	hardness of intact ice
B_f	— $\text{Pa s}^{-1/3}$	hardness of failed ice
β	$7.624 \times 10^6 \text{ Pa s/m}$	sliding coefficient
m	1/3	sliding law exponent
\dot{a}_0	0.75 m/a	dimensional accumulation rate
Δa	1 m/a	variation in accumulation rate
T	5000 a	period accumulation change
b_0	260 m	bed elevation at $x = 0$
α	0.017	bed slope
b_1	350 m	height of bump in the bed
x_0	40 km	center of bump in the bed
σ	10 km	width of bump in the bed

Table 1. Numerical values of parameters used in different models. The hardness parameter of yielded ice is not used in any of the simulations.

Figure 6. Snapshots showing advance and retreat for the Plastic bed model (filled gray outline) and Perfect plastic approximation (dashed red lines).

Figure 7. Snapshots showing advance and retreat for the Weertman model (filled gray outline) and SIA model (dashed red lines).

Figure 8. Time series showing the evolution of terminus position (panel a), calving rate (panel b), terminus velocity (panel c) for a time varying accumulation rate (panel d). The black line shows the trajectory based on the Perfect plastic approximation model. The pink line shows the trajectory calculated using the Plastic bed model and the blue line shows the trajectory calculated using the Weertman model.

Figure 9. Bifurcation diagram showing terminus position as a function of accumulation rate for the Plastic bed model (black) and Weertman model (blue). Stable solutions are indicated using a solid black line for the Plastic bed model and dashed line for the Weertman model. Dotted lines show unstable branches. Circles denote bifurcation points where the solutions transition from stable to unstable. Panels a and b show solutions obtained for a yield strength $\tau_y = 150$ kPa and $\tau_y = 200$ kPa, respectively.

Figure 1.

Author Manuscript

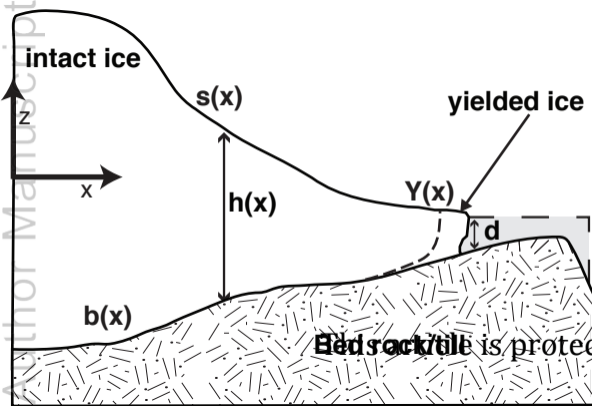


Figure 2.

Author Manuscript

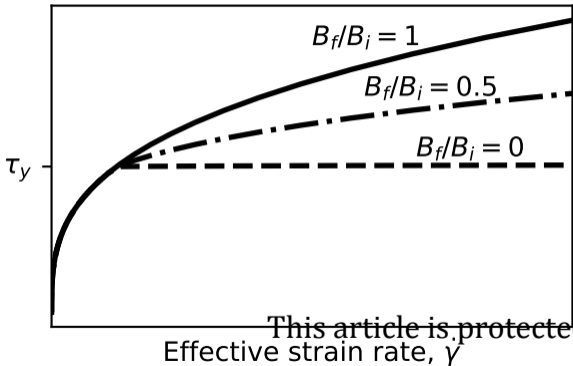
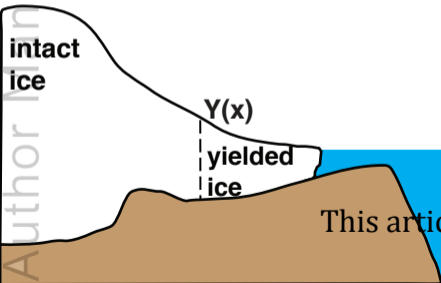


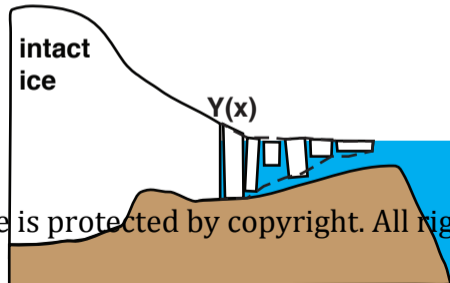
Figure 3.

Author Manuscript

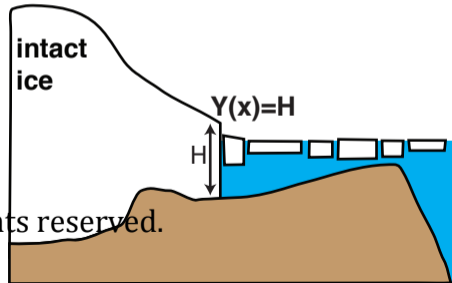
a) Yield surface separates intact ice from yielded (fractured) ice



b) Rapid flow of yielded ice thins to form a plug of floating mélange.



c) Mélange tongue of yielded ice thins rapidly exposing the yield surface as the calving front



This article is protected by copyright. All rights reserved.

Figure 4.

Author Manuscript

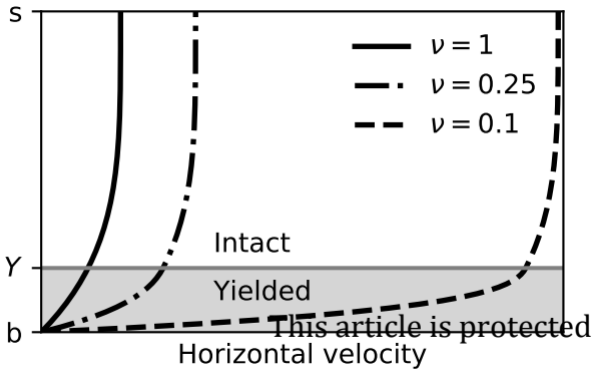


Figure 5.

Author Manuscript

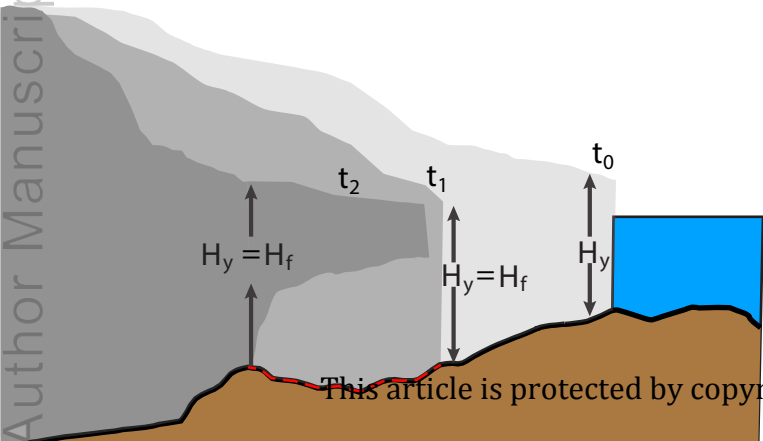


Figure 6.

Author Manuscript

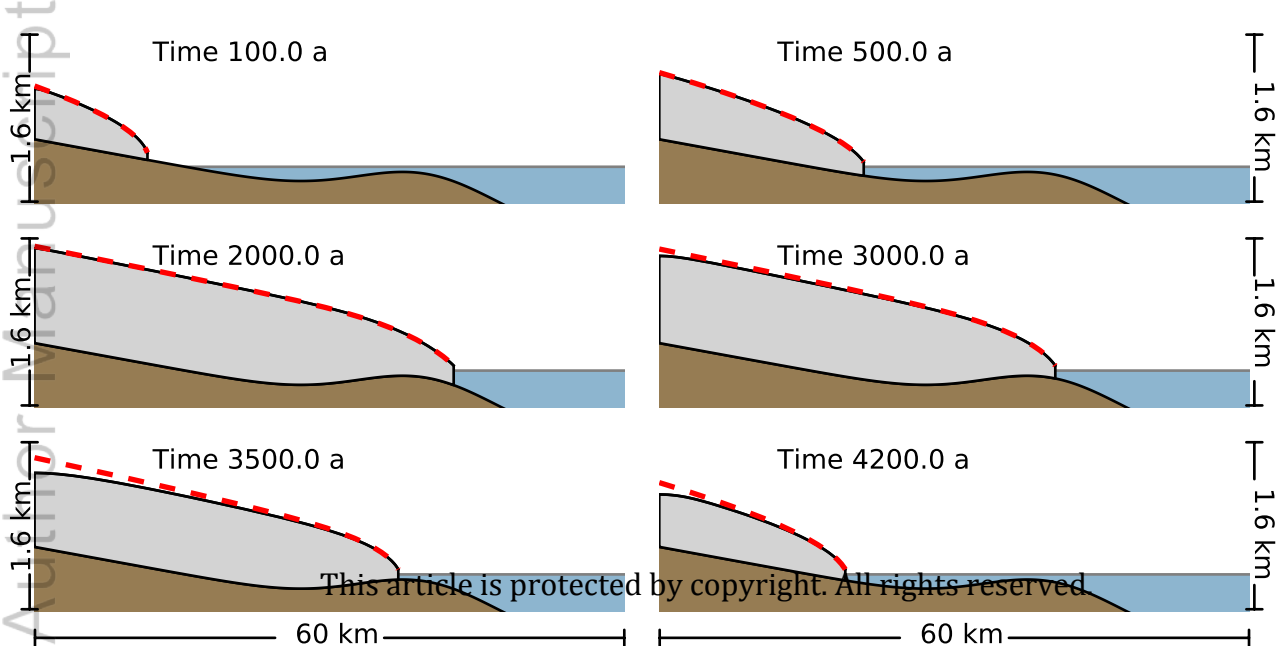


Figure 7.

Author Manuscript

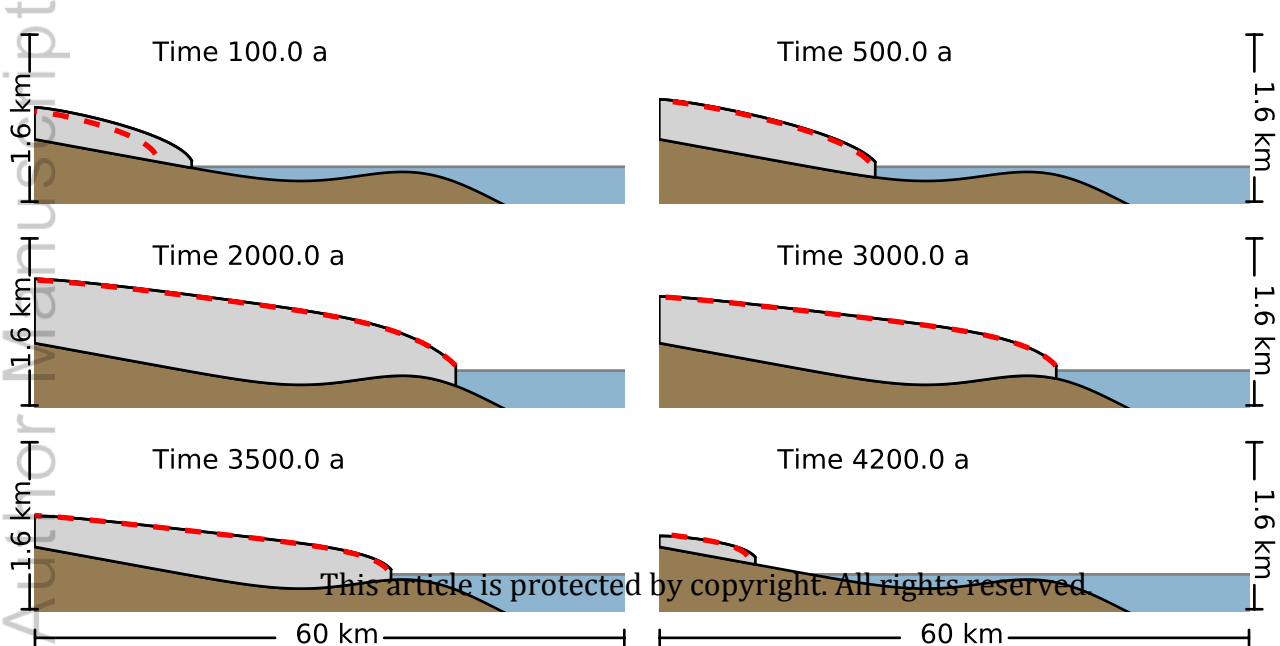


Figure 8.

Author Manuscript

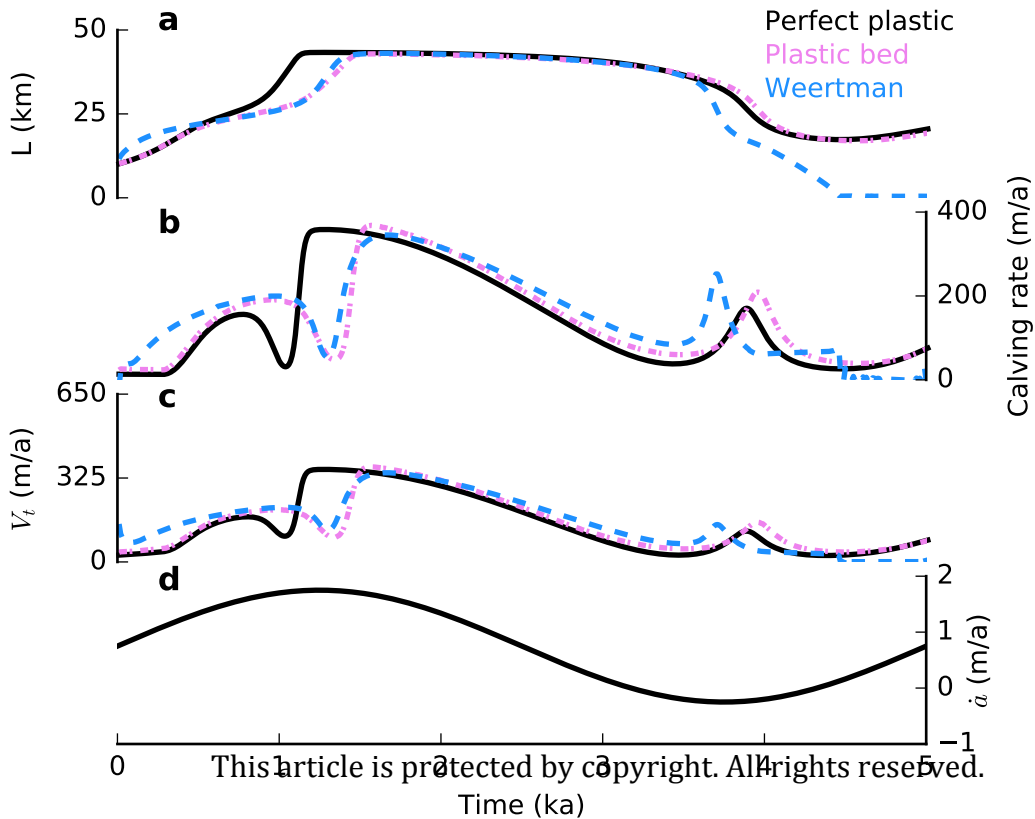
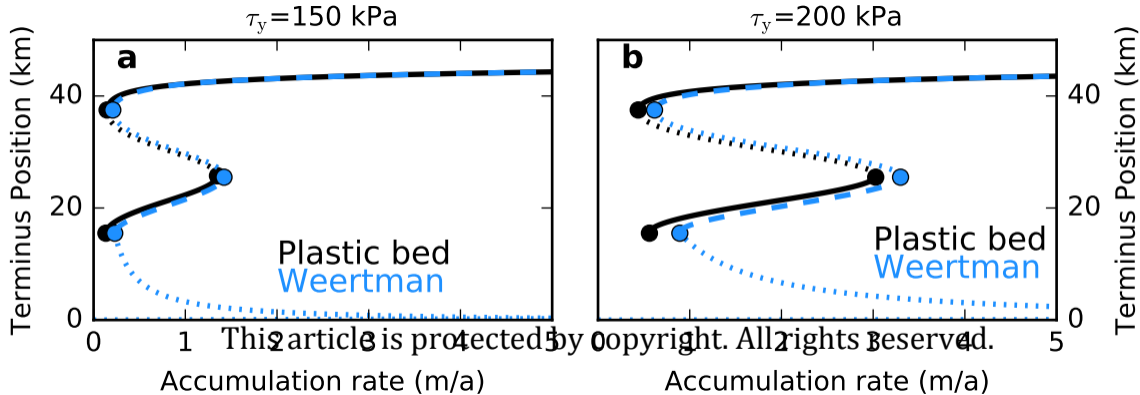
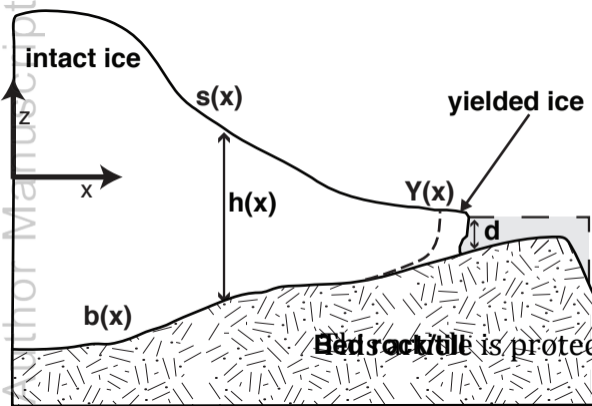
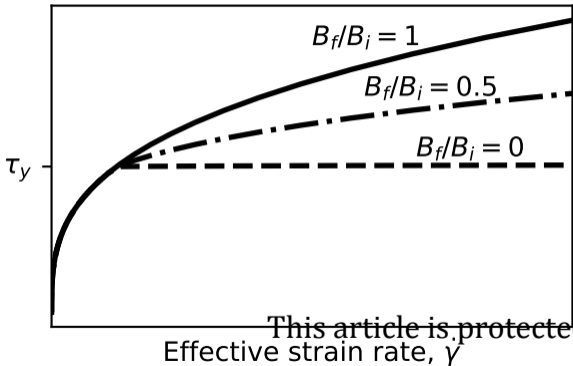


Figure 9.

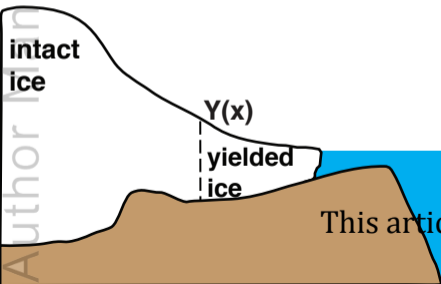
Author Manuscript



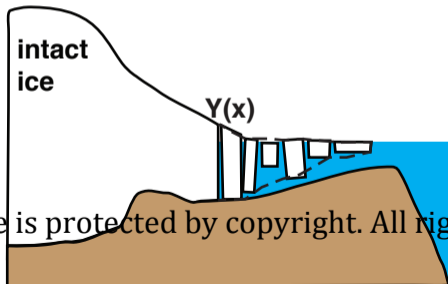




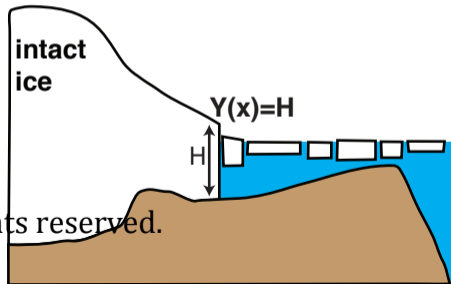
a) Yield surface separates intact ice from yielded (fractured) ice



b) Rapid flow of yielded ice thins to form a plug of floating mélange.



c) Mélange tongue of yielded ice thins rapidly exposing the yield surface as the calving front



This article is protected by copyright. All rights reserved.

